Self-Collimating SPECT With Multi-Layer Interspaced Mosaic Detectors

Tianyu Ma, *Member, IEEE*, Qingyang Wei, *Senior Member, IEEE*, Zhenlei Lyu,
Debin Zhang, Hongyang Zhang, Rui Wang, Jiahong Dong, Yaqiang Liu,
Rutao Yao, *Senior Member, IEEE*, and Zuo-Xiang He

Abstract—Conventional single photon emission computed tomography (SPECT) relies on mechanical collimation whose resolution and sensitivity are interdependent, the best performance a SPECT system can attain is only a compromise of these two equally desired properties. To simultaneously achieve high resolution and sensitivity, we propose to use sensitive detectors constructed in a multi-layer inter spaced mosaic detectors (MATRICES) architecture to accomplish part of the collimation needed. We name this new approach self-collimation. We evaluate three self-collimating SPECT systems and report their imaging performance: 1) A simulated human brain SPECT achieves 3.88% sensitivity, it clearly resolves 0.5-mm and 1.0-mm hot-rod patterns at noise-free and realistic count-levels, respectively; 2) a simulated mouse SPECT achieves 1.25% sensitivity, it clearly resolves 50-μm and 100-μm hot-rod patterns at noise-free and realistic count-levels, respectively; 3) a SPECT prototype achieves 0.14% sensitivity and clearly separates 0.3-mm-diameter point sources of which the center-to-center neighbor distance is also 0.3 mm. Simulated contrast phantom studies show excellent resolution and signal-to-noise performance. The unprecedented system performance demonstrated by these 3 SPECT scanners is a clear manifestation of the superiority of the self-collimating approach over conventional mechanical collimation. It represents a potential paradigm shift in SPECT technology development.

Index Terms—High resolution and sensitivity, SPECT, system design.

I. Introduction

SINGLE photon emission computed tomography (SPECT) is a well-established *in vivo* molecular imaging technology that is capable of detecting biological signals at sub-nanomolar level [1], [2]. However, from its inception [3], SPECT technology suffers fundamental limitations caused by mechanical collimation, the very component that enables gamma camera and SPECT imaging [4], [5].

Mechanical collimation yields an inherent inverse interdependency between a SPECT system's resolution and sensitivity. Usually constructed with a heavy metal such as lead or tungsten, a mechanical collimator confines the photon sensitive region through physical apertures that only allow photons within a selective angular range to pass through and absorb the rest. The sizes of the apertures determine both the selectiveness of the region, i.e. resolution, as well as the acceptance quantity from the region, i.e. sensitivity. A boost of resolution means a more constrained angular range therefore leading to a loss of sensitivity, and vice versa. This inverse interdependency defines the overall poor performance of the conventional SPECT systems.

The inherent limitation of mechanical collimation has severely hindered the progression of SPECT technology for many years. Although many different geometries of mechanical collimation have been investigated, as shown in Table I, the best performance of human body SPECT systems that use parallel hole collimators have a resolution inferior to 10 mm and sensitivity lower than 0.1%. For imaging human brain and heart, pinhole SPECT systems reports resolution of about 3 - 5 mm, also with a sensitivity of less than 0.1%. State-of-the-art small animal SPECT systems use multi-pinhole collimation to aim multiple small pinholes at a small field-of-view (FOV) to simultaneously gain efficiency from the sheer number of holes and improve resolution through magnification [6]. However, the interdependency between resolution and sensitivity remains for each pinhole and the small FOV makes it challenging to extend the approach to human imaging.

The resolution-sensitivity interdependency constraint persists for other variations of mechanical collimators including slit-slat collimator [7]–[9], which can be viewed as

TABLE I
RESOLUTION AND SENSITIVITY PERFORMANCE OF A FEW REPRESENTATIVE SPECT SYSTEMS REPORTED IN THE LITERATURE.

Collimation type	Imaging Subject	Resolution (mm)	Sensitivity (%)
Parallel-hole or fan-beam	Mouse [10]	1.2-1.6	0.0028-0.0032
	Heart [11]	8.6	0.085
	Brain [12]	7.4-8.9	0.0086-0.014
	Whole-body [11]	15.3	0.013
Multi pinhole	Mouse [13]	0.25	0.038
	Heart [14]	5.8	0.066
	Brain [12, 15, 16]	2.5-4.7	0.042-0.086
Slit-slat	Mouse [7]	1.0	0.0092-0.0196
	Heart [8]	11.0	0.06
	Brain[9]	6.0	0.051
Coded aperture	Mouse [17]	1.5	1.28

a combination of in-plane pinhole collimator and axial parallel-hole collimator; and coded-aperture collimator, which can be regarded as an extreme of a multi-pinhole collimator that has a large number of holes. Although coded-aperture collimators claim high sensitivity, a high fraction of its counts come from multiplexing, so it is only useful for imaging sparse objects [5].

To significantly improve the performance of SPECT technology, we propose a new collimation strategy termed (detector) self-collimation. The core concept is to replace part of the physical collimator with *spatially distributed sensitive detectors*. These detectors, while collecting photons useful for image formation, also constitute collimators that define the photon pathways to other detectors. With proper placement of the detectors, photon absorption on one detector forms the collimation for other detectors. This self-collimation setup enables detectors to perform dual functions of detecting gamma photons towards image generation and collimating for other detectors. This strategy opens the door to designing very high-resolution collimation without the loss of sensitivity.

In this work, we use a multi-layer interspaced mosaic detectors (MATRICES) architecture to implement the self-collimation strategy. To demonstrate the feasibility of the MATRICES based self-collimating SPECT, we carry out design studies of a human brain SPECT system and an animal SPECT system through Monte Carlo simulations. We also assemble a SPECT prototype as proof of concept.

II. MATERIALS AND METHODS

A. Self-Collimation Concept

The self-collimation concept is illustrated in Fig. 1. The conventional photon-absorptive metal collimator in Fig. 1(a)
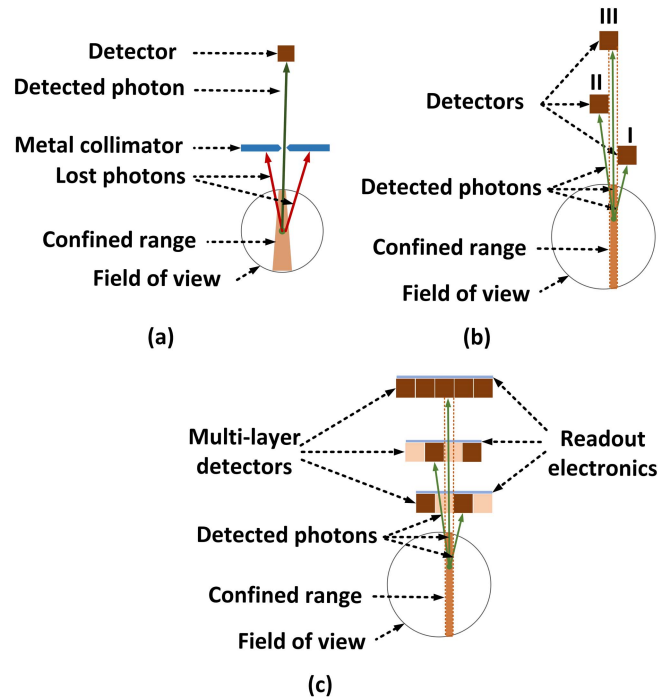

Fig. 1. Illustration of (a) conventional collimator, (b) the proposed self-collimation concept with three strategically placed individual detectors, and (c) self-collimation with three layers of mosaic detectors. The red lines indicate photons lost due to collimator absorption. The green lines indicate gamma photons detected by the imaging system.
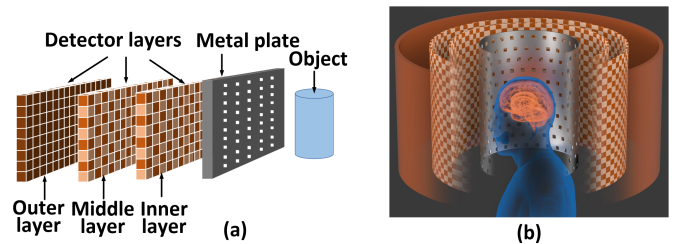

Fig. 2. Illustration of (a) a MATRICES module, and (b) a full-ring SPECT composed of MATRICES modules.

is replaced in Fig. 1(b) by two sensitive detectors, I and II, they effectively constitute a collimator to cast a photon pathway towards detector III. So, detector III collects photons *collimated by detectors* I and II. Because I and II are sensitive detectors, they also collect photons for the reconstruction of the emission image. Clearly, the roles of detectors I and II are quite different from that of the conventional mechanical collimators. In this way, higher resolution, i.e. more restrictive collimation, may be achieved not at the expense of sensitivity.

In Fig. 1(c), the three individual detectors are extended to three detector layers that consist of consecutive detector elements of two different scintillators, indicated by two colors, that are arranged in a *mosaic pattern*. The two types of scintillators selected should have different attenuation properties to act as collimators for casting photon pathways. A few candidate scintillators for this design are shown in Table II and the selection considerations are discussed in Section II.C.

Based on the concept shown in Fig. 1(c), Fig. 2(a) shows a MATRICES module which consists of three — namely outer, middle and inner — detector layers and a metal plate with

TABLE II
SCINTILLATOR MATERIAL PROPERTIES

Scintillator	Linear attenuation coefficient @ 140 keV(cm^{-1})[*]	Decay time (ns)[**]
Bismuth Germanate (BGO)	11.71	300
Lutetium Yttrium Orthosilicate (LYSO)	8.97	42
Gadolinium Orthosilicate (GSO)	6.36	60
Gadolinium Aluminum Gallium Garnet (Ce) (GAGG(Ce))	4.75	50 / 90[***]
Cesium Iodide (Tl) (CsI(Tl))	3.61	1000
Lanthanum Bromide (LaBr3)	2.66	35
Sodium Iodide (Tl) (NaI(Tl))	2.46	230
Yttrium Orthosilicate (YSO)	1.29	70

[*]Linear attenuation coefficients are from XCOM data base [20]. [**]Decay time of GAGG(Ce), LYSO and YSO are from our vendor's datasheet. Decay time of the rest of materials are from [21]. [***] The GAGG(Ce) materials provided by our vendor has two types with different decay time[22].

TABLE III
SCINTILLATORS USED IN SIMULATION AND PROTOTYPE

System	Inner-middle layers	Outer layer	Cross-sectional size of crystals
Simulated brain SPECT	GSO-YSO	GSO	2 mm × 2 mm
Simulated mouse SPECT	GAGG(Ce)-YSO	GAGG(Ce)	1 mm × 1 mm
Experimental prototype	LYSO-YSO	GAGG(Ce)	1.35 mm × 2.7 mm

apertures. The metal plate is between the image object and the inner, also the inner-most, detector layer, it provides photon collimation in a conventional way. It should be noted, however, this metal plate is only a fraction of the whole collimation scheme of a MATRICES architecture, its inherent limitation as a mechanical collimator affects mostly the inner detector only; therefore, the plate can be designed to allow a large fraction of photons to pass through. Fig. 2(b) shows a full ring version of a self-collimating SPECT composed of many MATRICES modules.

B. Assess Three MATRICES SPECT Systems

We investigate the performance of two simulated and a prototype MATRICES SPECT system to assess the validity and characteristics of the self-collimation concept. Scintillation detectors are used in all 3 systems. One simulated system has a FOV size of 200 mm (Ø)× 200 mm (L) to emulate a human brain scanner, the other has a FOV size of 30 mm (Ø)× 100 mm (L) to imitate a mouse imager. The two simulated systems are full-ring scanners and assessed for their resolutions, sensitivities and signal-to-noise performances. The prototype has a heptagonal detector geometry. Full details of each system are described in the following sections.

We use GATE V8.0 [18] as the simulation platform in this work. The imaging isotope used in all simulations and experimental tasks is ^{99m}Tc. In simulation studies and experiments, photon event data are acquired in the 120 – 160 keV energy window.

C. Scintillator Choices of MATRICES SPECT

The dual requirements for collimation and detection, for the inner and middle layer detectors illustrated in Fig. 2, make choosing MATRICES scintillators a brand-new challenge in system design. As an educated guess, we choose to use two types of scintillators with a strong contrast of attenuation properties to form scintillator-pairs to construct MATRICES modules.

Table II lists a few candidate scintillators ordered from high to low by their linear attenuation coefficients. We may choose one scintillator from the top four rows and one from the bottom four rows to form scintillator pairs. BGO, CsI(Tl), LaBr$_3$ and NaI(Tl) are excluded for practical considerations: the low light-yield and long decay-time of BGO would lead to a low signal amplitude in the readout electronics for low energy photons of 140 keV; CsI(Tl), LaBr$_3$ and NaI(Tl) have hygroscopic tendency which makes them vulnerable for potential prototype development.

To experiment with different scintillator-pairs, the detectors on the inner and middle layers of the simulated brain, simulated mouse, and the prototype MATRICES SPECT systems are constructed with GSO-YSO, GAGG(Ce)-YSO, and LYSO-YSO respectively. Because outer layer detectors perform only photon-detection function, we use one scintillator type with high linear attenuation coefficient, instead of a pair of scintillators with contrast, in this layer: GSO for the brain SPECT, GAGG(Ce) for the mouse SPECT, and GAGG(Ce) for the prototype. On the prototype, we apply a background subtraction approach to correct for the intrinsic ^{176}Lu radiation [19] for inner and middle layer detectors, of which the relatively high sensitivity to imaging source activity provides statistically adequate signals. Because outer layer detectors have a low sensitivity to imaging source, a scintillator free of intrinsic radiation is strongly preferred, so we choose GAGG(Ce).

In system simulations, we set the energy resolutions for GAGG(Ce) [23], GSO, and YSO detectors at 21%, 20% and 18% respectively for gamma photons at 140 keV. These values are based on the measured results in our lab. Our measured energy resolutions for GSO and YSO are close to those reported in literature [24], [25].

D. Geometrical Parameters of MATRICES SPECT

The geometrical parameters defining the simulated MATRICES brain and mouse SPECT systems are illustrated in Fig. 3. The preselected widths of both types of crystals on the brain SPECT are $w_2 = w_3 = w_4 = 2$ mm, and $w_2 = w_3 = w_4 = 1$ mm on the mouse SPECT (Table III). The cross-section of all the crystals is square-shaped. The width of the square apertures w_1 on the metal plate is chosen to match the crystal width on the system. Several other parameters are also pre-selected: the height of the scintillator ring is the same as the target axial FOV, i.e. $H = 200$ mm in the brain SPECT and $H = 100$ mm in the mouse SPECT. The metal plate is made of tungsten, its radial thickness is $t_1 = 2$ mm (which allows < 5% penetration for photons at
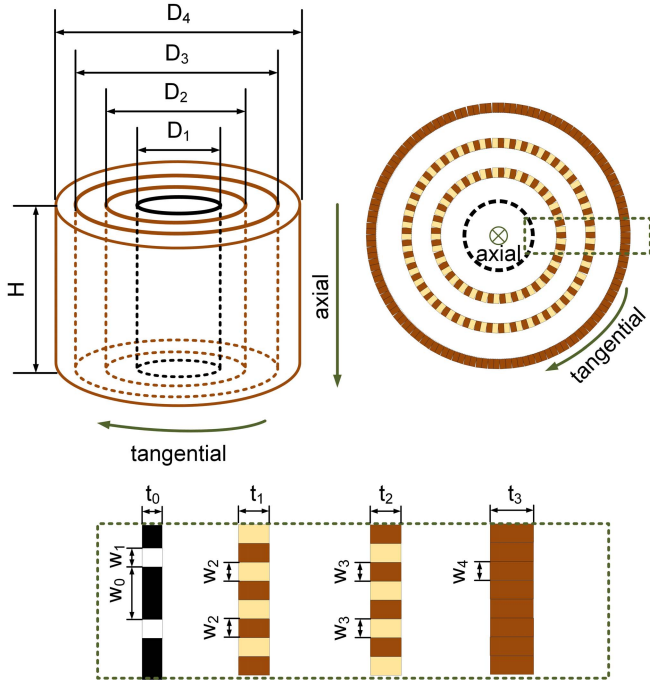
Fig. 3. Illustration of a ring-shaped MATRICES system and its geometrical parameters. Left: 3-D perspective view. Top right: top view. Bottom: close-up view of the segment within the dashed-line rectangle in the top-right diagram.

140 keV). The radial thickness of outer layer scintillators is $t_4 = 7$ mm (which allows $< 4\%$ penetration for photons at 140 keV). The inner diameter of the metal ring is $D_1 = 382.0$ mm in the brain SPECT and $D_1 = 38.2$ mm in the mouse SPECT respectively. The inner diameter of the outer detector ring is $D_4 = 1018.6$ mm in the brain SPECT and $D_4 = 509.3$ mm in the mouse SPECT (to accommodate an even number of 1600 scintillators in both systems).

The rest of the geometrical parameters of the two simulated SPECT systems are optimized based on the well-established uniform Cramer-Rao bound approach [26]–[30], which evaluates the resolution-variance tradeoff for each specific system parameter-set to choose a preferred parameter value. Below is a brief description of the approach.

Following the system performance characterization method in [27], the variance bound B and corresponding bias-gradient length δ for the n-th voxel in the vector θ, which is a uniform image distributed over the entire FOV, are respectively expressed as:

$$B_n(\boldsymbol{\theta}, \lambda) = \lambda^2 \boldsymbol{e}_n^T (\boldsymbol{I} + \lambda \boldsymbol{F}_\theta)^{-1} \boldsymbol{F}_\theta (\boldsymbol{I} + \lambda \boldsymbol{F}_\theta)^{-1} \boldsymbol{e}_n \quad (1)$$

$$\delta_n(\boldsymbol{\theta}, \lambda) = \left\| (\boldsymbol{I} + \lambda \boldsymbol{F}_\theta)^{-1} \boldsymbol{e}_n \right\|, \quad (2)$$

$$\boldsymbol{F}_\theta = \boldsymbol{A}^T [\text{diag}(\boldsymbol{A}\boldsymbol{\theta})]^{-1} \boldsymbol{A}, \quad (3)$$

where λ is a non-negative scalar, $\boldsymbol{I}$ is an identity matrix, $\boldsymbol{e}_n$ is a vector that has the same size of θ with all the elements being zero except that the n-th element is 1, $\boldsymbol{F}_\theta$ is the Fisher information matrix, $\boldsymbol{A}$ is the system response matrix calculated through a numerical multi-ray-tracing method. No background is accounted for in this method.

We further define the average deviation bound κ,

$$\kappa = \sum_{n=1}^{N} \sqrt{B_n(\theta, \lambda)} \Big/ N \quad (4)$$

where N is the total number of voxels in the targeted FOV.

The average deviation bound κ and bias-gradient length δ can be approximately interpreted as noise and resolution magnitudes, respectively. By sweeping λ from 0 to $+\infty$, the relationship of κ *vs.* δ is quantitatively characterized and we use it as the figure-of-merit for optimizing selected parameters.

1) Simulated Human Brain SPECT: Using the approach described above, but only for a single-plane FOV to make the computational requirement manageable, we determine the following brain system parameters: the aperture opening ratio r, the inner diameters of inner and middle layers, D_2 and D_3, and the radial thickness of inner and middle layers, t_2 and t_3. The definition of r is $r \triangleq w_1/(w_1 + w_0)$, where w_0 is the width of the tungsten section between neighboring apertures (Fig. 3). We optimize each of the above parameter(s) one at a time by identifying the parameter value that achieves a desired κ *vs.* δ performance. The steps are:

1) Set $D_2 = 594.2$ mm and $D_3 = 806.4$ mm, i.e. the inner and middle detector layers are evenly spaced between the metal layer ($D_1 = 382.0$ mm) and the outer layer detector ($D_4 = 1018.6$ mm).
2) Set $t_2 = t_3 = 3.5$ mm, i.e. the inner and middle layer scintillators have half the thickness of the outer layer scintillator.
3) Set $w_1 = 2$ mm, i.e. the width of the square apertures on the metal plate equals the width of the detector crystals.
4) Calculate κ *vs.* δ curves for r *values* ranging from 1/10 to 1/2 (change w_0, with w_1 fixed). The optimal r value yields the lowest curve.
5) With the optimized r identified, calculate κ *vs.* δ curves to search for the optimal (D_2, D_3) in the range $D_1 < D_2 < D_3 < D_4$.
6) With the optimized r, D_2 and D_3 identified, calculate κ *vs.* δ curves to search for the optimal (t_2, t_3) in the range $\{1 \text{ mm} \leq t_2 \leq 7 \text{ mm}, 1 \text{ mm} \leq t_3 \leq 7 \text{ mm}\}$.

We run the optimization steps 4) to 6) twice and obtain following values: $r = 1/3$, $D_2 = 560.2$ mm (880 scintillators), $D_3 = 611.2$ mm (960 scintillators), and $t_2 = t_3 = 4$ mm. Fig. 4(a) shows the κ vs. δ curves with different collimator opening ratio r values ranging from 1/10 to 1/2. The chosen value r of 1/3 yields an optimal trade-off between sensitivity (favoring larger r) and resolution (favoring smaller r).

In most cases (except for the extreme case $r = 1/10$), the κ vs. δ curves clearly do not intersect with each other. This is also true in most of other studies we have performed. Therefore, we only show κ at a fixed δ as the representative of the system performance in the rest of the studies. Fig. 4(b) shows κ at a fixed δ as a function of the aperture width w_1. The figure reveals the trade-off between a better resolution (favoring smaller w_1) and a better sensitivity (i.e. lower κ, favoring larger w_1). The value we choose in the study, $w_1 = 2$ mm, is a choice that yields relatively low κ value as desired.
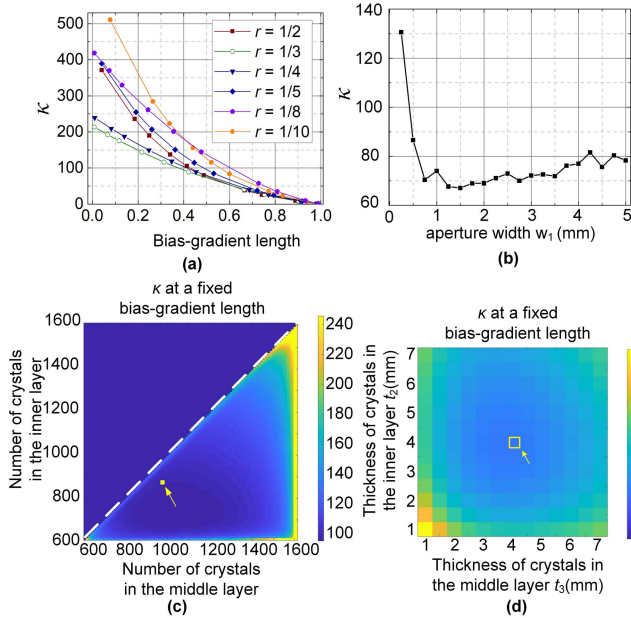
Fig. 4. Optimization of system parameters of the brain SPECT. (a) κ vs. δ curves for different opening ratio r values. (b) κ at a fixed δ, as a function of aperture width of the metal plate. (c) κ at a fixed δ, shown in a 2-D image, as a function of crystal numbers in the inner and middle layers. Note that the upper-left region above the dashed line should not be considered according to geometry definition. (d) κ at a fixed δ, shown as a 2-D image, as a function of inner and middle layer crystal depths.
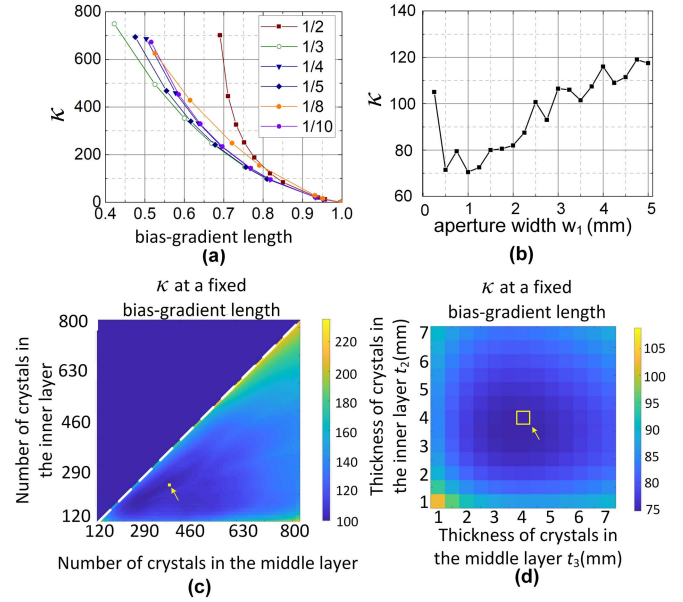
Fig. 5. Optimization of system parameters of the mouse SPECT. (a) κ vs. δ curves for different opening ratio r. (b) κ at a fixed δ, as a function of aperture width of the metal plate. (c) κ at a fixed δ, shown in a 2-D image, as a function of crystal numbers in the inner and middle layers. Note that the upper-left region above the dashed line should not be considered according to geometry definition. (d) κ at a fixed δ, shown as a 2-D image, as a function of inner and middle layer crystal depths.

Fig. 4(c) shows, at a fixed δ, κ values in a 2-D image with the numbers of crystals on the inner and middle layers (proportional to the corresponding ring diameters) being the row and column indices respectively. Note the upper-left half of the image should be ignored as the middle ring must be larger than the inner ring. In this image, a low κ zone is identified. The numbers of crystals in the zone reaches a balanced collimation-detection dual function. The chosen (D_2, D_3) are within the low κ zone.

Fig. 4(d) shows the dependence of κ (mapped to colors in a 2-D image) on the crystal thicknesses of the inner and middle layers. As the last optimization step, the chosen 4-mm thickness for both layers yields the lowest κ value.

We assume the optimized in-plane metal-plate parameters are applicable to the configuration in the axial direction. Henceforth we choose the aperture size of the metal plate to be 2 mm × 2 mm, and the center-to-center distance between adjacent 2-mm apertures to be 6 mm in the axial direction.

2) Simulated Mouse SPECT: Using the same κ vs. δ approach and steps described for optimizing the brain SPECT configuration in the last section, the geometrical parameters of the mouse SPECT are determined. II-D.3 shows the mouse SPECT optimization study results presented in the exact same arrangement as that of Fig. 4. The chosen values of the parameters are: the aperture opening ratio r is 1/3, the width of the apertures w_1 is 1 mm, the widths of the thickness of scintillators in inner and middle layer, t_3 and t_4, are both 4 mm, the widths of scintillators w_2, w_3, and w_4 are all 1 mm, the inner diameters of the metal ring and outer-layer detector are 38.2 mm and 509.3 mm,

respectively. Correspondingly, the diameters of the inner (D_2) and middle (D_3) detector layers are 76.4 mm and 114.6 mm, and the system has 240, 360 and 1600 scintillators in the inner, middle and outer layer detectors respectively in each trans-axial detector plane.

3) Experimental Prototype: We build a MATRICES SPECT prototype to experimentally test the self-collimation concept. As shown in Fig. 6, the prototype consists of 7 detector modules (Fig. 6 (a)) forming a heptagon, and an object support and movement stage (inside the heptagon). An image object, such as a point source as shown in Fig. 6 (b), can be rotated about the vertical axis and translationally moved in the FOV. The side and top views of a MATRICES module with the corresponding covers removed are shown in Fig. 6 (c) and (d) respectively. Each MATRICES module consists of a tungsten metal plate with square holes (Fig. 6 (e)) and three detector layers. Matching the design geometry of the simulated mouse SPECT, the plate is 2 mm thick, the holes are 1 mm × 1 mm in size with 3 mm center-to-center intervals, and the central plane of the plate is 19.1 mm from the center of FOV. Each detector layer of a MATRICES module consists of two scintillator blocks. Each block consists of 24 × 24 scintillators. Fig. 6 (f) and (g) are pictures of two individual scintillator blocks, each block is read out by an 8 × 16 SiPM array (FJ30035, ON Semiconductor, USA) and an ASIC developed by our group [23], [31]–[34]. The active area for each SiPM unit is 3 mm × 3 mm. There is a total of four data processing boards (DPBs) for digitizing position and energy signals. All the DPBs are connected to a switch, with which all the signals are transferred to a computer.

TABLE IV
SUMMARY OF GEOMETRY PARAMETERS, COUNTING STATISTICS, AND COMPUTING HOURS INVOLVED IN GENERATING THE SYSTEM MATRICES

| System	FOV	Voxel size	Number of voxels	Number of detector bins	Average recorded events per voxel	Approximate total CPU hour	Storage
Single plane brain SPECT,	200 mm ($\hat{\Phi}$ × 0.25 mm (L)	0.25 mm × 0.25 mm × 0.25 mm	640,000	10,320	6.5 M	8,400	24.6 GB
Brain SPECT, w/o water medium	80 mm ($\hat{\Phi}$× 6 mm (L)	0.8 mm × 0.8 mm × 0.4 mm (axial)	150,000	247,680	3.7 M	116,000	184.5 GB
Brain SPECT, with water medium	80 mm ($\hat{\Phi}$× 6 mm (L)	0.8 mm × 0.8 mm × 0.4 mm (axial)	150,000	247,680	1.8 M	62,000	184.5 GB
Single plane animal SPECT	10 mm (Φ) × 10 μm (L)	10 μm × 10 μm × 10 μm	100,000	6,600	1.6 M	7,500	24.6 GB
Animal SPECT	8 mm (Φ) × 5 mm (L)	12.5 μm × 12.5 μm × 12.5 μm	163,840	660,000	15.4 M	40,000	402.8 GB
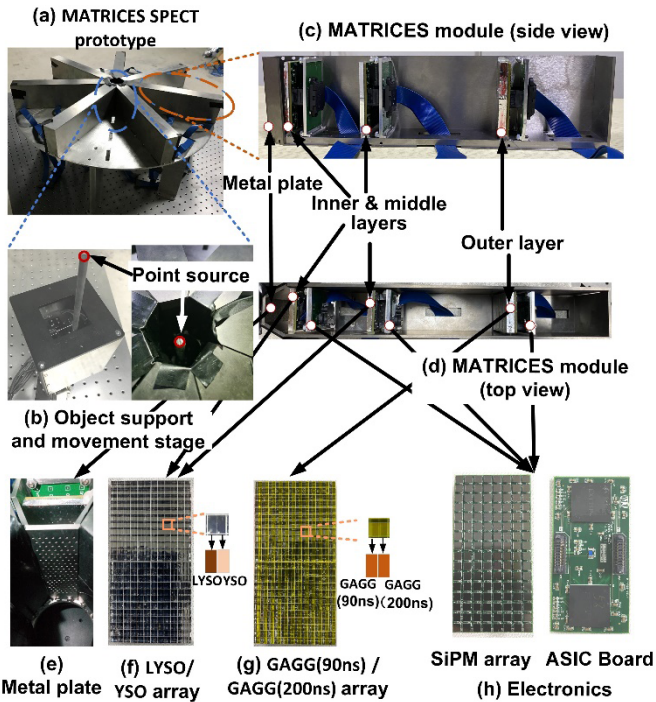
Fig. 6. Pictures of the MATRICES SPECT prototype which consists of (a) seven MATRICES modules forming a heptagon FOV, (b) an object support and movement stage at the center of the FOV. The components in a MATRICES module are shown in (c)–(g).

The tangential cross-section of the scintillators is 1.35 mm × 2.7 mm, the smallest resolvable size with the electronics developed by our group. The LYSO-YSO scintillator pair used in the inner and middle layers have different decay times (LYSO - 42 ns, and YSO -70 ns), which allow us to resolve 1.35 mm (tangential) × 2.7 mm (axial) crystals using the phoswich approach [23] and hence improves detector intrinsic resolution in tangential direction. In the outer layer, we also use two different types of GAGG crystals with 50 ns and 90 ns decay time, and therefore the resolvable crystal size is also 1.35 mm (tangential) × 2.7 mm (axial). The crystal thickness (radial) is 4 mm for the inner and middle layers, and 7 mm for the outer layer, same as those of the simulated mouse SPECT.

When a scintillator is activated by a photon event, the scintillator type is identified first by a pulse-shape discrimination method based on the area-to-peak ratio of the scintillation light signal [23]. Then the centroid value of the photon event is calculated with the built-in anger-logic resistor network in the ASIC. The crystal index is determined using the pre-stored crystal identification look-up table. Crystal index calculation and energy window discrimination are processed off-line.

The SiPM board and the ASIC board, Fig. 6 (h), are behind the scintillator arrays. According to our measurement, photon absorption by the boards of the inner and middle layer detector electronics causes 10% - 20% loss of 140 keV photons.

E. Projection Data and System Response Matrix

We concatenate all projection events into a single vector

$$Y = [y_{1,inner}, \ldots, y_{N1,inner}, y_{1,middle}, \ldots,$$
$$y_{N2,middle}, y_{1,outer}, \ldots, y_{N3,outer}]^T, \quad (5)$$

where $y_{i,l}$ is the number of events acquired by detector-element i on detector-layer l; N_1, N_2 and N_3 are the numbers of scintillators in the inner, middle and outer layers respectively. Correspondingly, the concatenated system response matrix is

$$P = \begin{bmatrix} P_{inner} \in \mathbb{R}^{N1 \times M} \\ P_{middle} \in \mathbb{R}^{N2 \times M} \\ P_{outer} \in \mathbb{R}^{N3 \times M} \end{bmatrix} \in \mathbb{R}^{(N1+N2+N3) \times M}, \quad (6)$$

where M is the total number of voxels in the FOV. The system matrices for the simulated systems are derived from Monte Carlo simulations of uniform sources that fill the FOVs [35]. Table IV summarizes the geometry parameters, the counting statistics, and the computational hours involved.

In this way, the combination of projections from different layers are used in image reconstruction in a unified framework. Similar approaches have been used in PET that combine data measured from high-resolution and low-resolution detectors [36], [37].

1) Simulated Human Brain SPECT: To test the best achievable resolution with our available computational resource, we generate the system matrix for the central image plane of the FOV with a high-resolution voxel size setting of 0.25 mm × 0.25 mm × 0.25 mm.

To evaluate the imaging performance in terms of contrast and noise, we derive a system matrix in a limited FOV,

i.e. 80 mm (Ø)× 8 mm (L) and with a relatively large voxel size, i.e. 0.8 mm × 0.8 mm × 0.4 mm (axial). Though the simulated system is 200 mm long in axial direction, we only store the event in the central part of the system containing 15 axial slices (6 mm long). The above setup produces a 150,000 × 247,680 matrix, as listed in Table IV. We run the simulation twice — by placing the source first in air, and then in a water-filled phantom to evaluate the impact of photon attenuation and scattering. The water phantom is 250 mm (Ø)× 50 mm (L) in size. Its diameter mimics the size of a human head, and its axial length is slightly larger than the central part of the system that actually impacts the volume of interest. The simulated matrix used for the water-filled phantom study is generated with photon attenuation and scattering effects, thus by using this system matrix in the reconstruction, "ideal" attenuation and scatter corrections are implemented.

2) Simulated Mouse SPECT: Similar to that for the human brain system, we derive a system matrix first for a single plane 10 mm (Ø)× 10 μm (L) FOV and with a 10 μm × 10 μm × 10 μm voxel size for resolution evaluation, then a system matrix with an image FOV of 8 mm (Ø)× 5 mm (L) and a voxel size of 12.5 μm × 12.5 μm × 12.5 μm for contrast and noise evaluation. Photon attenuation and scattering are not considered in the mouse SPECT system.

3) Prototype SPECT: The system matrix of the prototype system is measured by moving a ^{99m}Tc point source (AG® 1-X8 Anion Exchange Resin, Bio-Rad laboratories, Inc, USA) [38] attached to the object support and movement stage as shown in Fig. 6 (b). We perform the measurement scan for 6 rounds. In each round we use a new point source and measure the system matrix at a different location. The diameter of the point source, the smallest we can make in our lab, is 0.3 mm, and the activities of the newly loaded point sources range from 1.8 mCi to 2.5 mCi. At each location, we scan a 1.35 mm × 1.35 mm × 0.75 mm range over a 10 × 10 × 6 grid pattern with a 0.15 mm grid-step size. The measurement time at each step is gradually increased to compensate for the decay of ^{99m}Tc activity. A total of 1.2 × 10^9 ~1.5 × 10^9 events is acquired in ~ 6 hours in each round. We interpolate the acquired system matrix on the 10 × 10 × 6 scan grid in the image domain to that on a 20 × 20 × 12 image grid through cubic spline interpolation, so the eventual voxel size of the system matrix is 75 μm × 75 μm × 75 μm.

F. Phantom Studies

1) On the Simulated Human Brain SPECT: Two in-air line sources, one placed over a trans-axial and the other over the axial axis, are simulated to evaluate the system's sensitivity profile. The line sources are 0.01 mm in diameter, and their lengths equal to the sizes of FOV in trans-axial and axial directions respectively. In the simulation, we acquire ~10^8 counts in each case. Each line source is virtually divided into 50 bins along its longitudinal direction. The sensitivity in each bin is simply the ratio of the acquired counts to the total emitted photons in the bin.

We evaluate the spatial resolution performance with a planar hot rod phantom. It consists of 6 sectors with hot
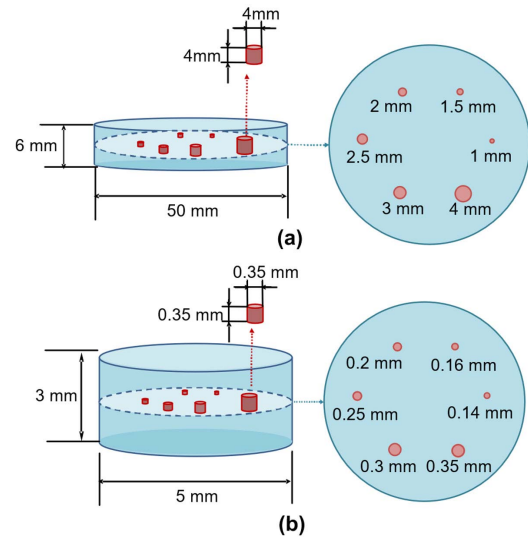

Fig. 7. Diagrams showing the simulated contrast phantoms scanned on the (a) brain and (b) mouse SPECT.

rods in different diameters, which are 0.5, 0.6, 0.75, 1.0, 1.2 and 1.5 mm respectively. There is no background activity between the hot rods, and the distances between the hot rods are twice their diameters. A total of 2 mCi activity is in the phantom. A tomographic scan consists of 3 rotational moves in 0.6° interval of the metal collimator ring combined with 4 × 4 translational moves (0.25 mm per step) of the phantom to achieve better spatial sampling [39], [40]. We simulate four imaging time cases, which are 510 hr (to mimic a nearly noise-free case), 5 hr, 50 min and 12.7 min and correspond to a total of 5.3 × 10^{12}, 5.2 × 10^{10}, 8.6 × 10^9 and 2.2 × 10^9 events in the projection, respectively. A tomographic scan with a total of 3 (collimator rotations) × 4 × 4 (translation moves) = 48 scan steps is performed in each case.

We carry out two contrast phantom studies. As shown in Fig. 7(a), the phantom has 6 hot cylindrical inserts (1, 1.5, 2, 2.5, 3, and 4 mm respectively in both diameters and lengths) in a 50 mm (Ø)× 6 mm (L) cylinder with a warm-background. The concentration ratio of all the hot cylinders to the background is 5:1. In the first study, the phantom is scanned in air. In the second study, the phantom is scanned in a 250 mm (Ø)× 50 mm (L) cylinder filled with water. In both studies, the phantoms are placed at the center of FOV and scanned with 3 rotational moves (0.6° interval) of the metal collimator ring and 2 × 2 × 2 translational steps (step size of 8 mm in the trans-axial directions and 1 mm in the axial direction) for a total of 24 scan steps. Projection data at four different count levels are simulated by imaging for 7.5 hr, 100 min, 5 min and 50 s respectively.

2) On the Simulated Mouse SPECT: With similar setup and steps as that for the brain SPECT, two in-air line sources, one placed over a trans-axial and the other over the axial axis, are simulated to evaluate the mouse SPECT system's sensitivity profile.

We scan a planar hot rod phantom consisting of 6 sectors with hot rods in different diameters, which are 50, 60, 70,

80, 100 and 120 μm respectively. There is no background activity between the hot rods, and the distances between the hot rods are twice their diameters. A total of 2 mCi activity is in the phantom. A tomographic scan of the phantom consists of three 0.6° rotational movements of the metal collimator ring, and 16 translational movements of the phantom over the cross-points on a 4 × 4 grid, each movement is a step of 60 μm in one direction. We simulate three imaging time cases, which are 660 hr (to mimic a nearly noise-free case), 20 hr and 20 min and correspond to a total of 2.2×10^{12}, 6.7×10^{10}, and 1.1×10^{9} projection counts respectively. A tomographic scan with a total of 3 (collimator rotations) × 4 × 4 (translation moves) = 48 scan steps is performed in the simulated imaging time.

A contrast phantom study similar to that for a human brain SPECT scan is performed. The phantom, shown in Fig. 7(b), has 6 hot cylindrical inserts (0.14, 0.16, 0.2, 0.25, 0.3, and 0.35 mm in both diameter and length) in a 5 mm (Ø)× 3 mm (L) cylinder with warm background, the ratio of activity concentrations in hot inserts to the background is 5:1. The phantom is placed in air and scanned with 3 rotational moves (0.6° interval) and 2 × 2 × 2 translational steps (step size of 0.5 mm in all three directions). Projection data at four different count levels are simulated, corresponding to scanning the phantom with the 3 (collimator rotations) × 2 × 2 × 2 (translational moves in three directions) = 24 scan steps in 20 hr, 7.5 hr, 1 hr and 20 min.

3) On the SPECT Prototype: After each round of the system matrix measurement (see Section II.E.3), the same point source used is scanned at the cross-points on a 3 × 3 × 2 grid pattern with three grid-step sizes: 0.6-mm, 0.45-mm, and 0.3-mm. This is equivalent to having 3 point-source phantoms, each has a different center-to-center distance between neighboring point-sources. The two with center-to-center distances shorter than the conventional configuration (twice of the point-source diameter) are to demonstrate the high-resolution of the prototype system. At each grid point, a 2 × 2 × 2 translational movement is implemented, with a 0.2 mm step-size in trans-axial (x and y) directions and 0.1 mm step-size axially. The acquired counts in each round of experiment are $1.2 \times 10^{8} \sim 1.3 \times 10^{8}$. The acquisition time at each point-source position is adjusted to compensate for ^{99m}Tc tracer decay. Combing the acquired list-mode events into a single dataset provides the projection data of a 3 × 3 × 2-point-source phantom.

Since the activity of the point source used in each round of scan is slightly different, for fair comparison, we extract a portion of acquired list-mode data from each round of measured dataset to match the case in which the point source has the lowest source activity. The dataset used in reconstruction thus mimics the case of scanning the 3 × 3 × 2-point-source phantom with a total of 0.32 mCi activity for 2 h (acquired 1.2×10^{8} total counts). We further generate the projection data at four different count levels, mimicking the measurement of the 3 × 3 × 2-point-source phantom with 0.3-mm grid-step size in 1 hr (6×10^{7} total counts), 15 min (1.5×10^{7} total counts) and 7.5 min (7.5×10^{6} total counts).

G. Reconstruction Settings

We use the ordered subset expectation maximization (OS-EM) algorithm [41] for image reconstruction. The reconstruction program is developed in MATLAB R2017b and runs on a workstation with intel E5-2680 CPU, 576 GB memory and a Nvidia GTX 1080 GPU card with 8 GB GPU memory. All reconstruction tasks use 120 subsets. The system matrix for each subset is fully stored in the GPU memory. In this way, the forward- and back-projection calculations are implemented with a straightforward matrix-vector multiplication. We run the reconstruction until convergence and then perform post-filtering with an empirically chosen Gaussian filter.

In both simulation and experimental studies, the voxel size in the image reconstruction matches that in the corresponding system matrix.

H. Image Quality Metrics

We calculate the contrast-to-noise ratio (CNR) of the hot rods to quantitatively evaluate image quality. It is defined as:

$$CNR_j = \frac{C_{H,j}/C_B - 1}{SD_B/C_B}, \tag{7}$$

where $j = 1, 2, \ldots, 6$ is the hot rod index, $C_{H,j}$ is the average image voxel value in the ROI of the j-th rod with the voxels on the edge of the hot rod excluded, C_B and SD_B are the average and standard deviation of the image voxel values respectively in the background ROI. The background ROI includes all the voxels in the warm background except those near the edge of the phantom or near the hot rods.

III. RESULTS

A. Sensitivity

1) Human Brain SPECT: The top-row of III-A.3 shows the sensitivity profiles of the simulated brain SPECT system in trans-axial and axial directions. The sensitivity values range from 3.45% to 4.87% with an average of 3.88% over the FOV. The average sensitivities of the inner, middle and outer detector layers are 2.58%, 0.86% and 0.44% respectively.

2) Simulated Mouse SPECT: For the mouse SPECT, the sensitivity values range from 0.90% to 2.78% and has an average of 1.25% over the FOV, as shown in the bottom-row of Fig. 8. The average sensitivities of the inner, middle and outer detector layers are 0.82%, 0.32% and 0.11% respectively. Compared to the brain SPECT system, the lower sensitivity and more prominent changes over the trans-axial and axial range here are due to the mouse SPECT's detector geometry — its FOV is more elongated in the axial direction and there are more photons incident towards the MATRICES in oblique angles which may be more likely absorbed by the metal plate.

3) Prototype SPECT: The sensitivity profiles of the prototype SPECT are shown in Fig. 9. The average sensitivity over all the measured points is 0.14%.

B. Projection and Scintillator Response Function

Fig. 10 shows the projection images of a 5 mm (Ø)× 3 mm (L) cylindrical source on the simulated mouse SPECT.
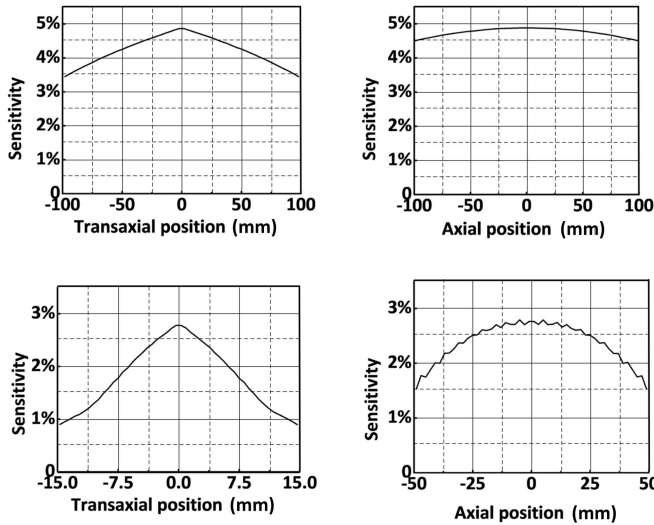
Fig. 8. Sensitivity profiles over the central trans-axial (left) and axial (right) axis. Top row: human brain SPECT. Bottom row: Mouse SPECT.
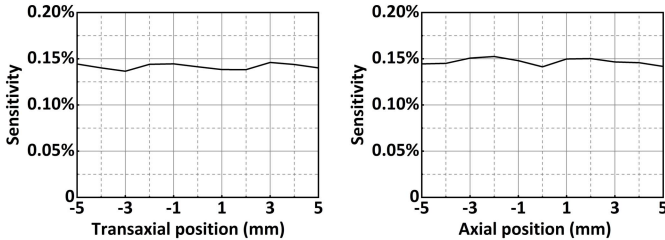

Fig. 9. Sensitivity profiles over the central trans-axial (left) and axial (right) axis for the SPECT prototype.

The projections of the inner and middle layer show clearly mosaic patterns, as a result of the mosaic detector design in these two layers.

We evaluate the scintillator response functions (SRFs), i.e. the response functions of individual scintillators, on the 3 SPECT systems to understand the underlying mechanism of the self-collimating concept. Each SRF is a row of the corresponding system matrix converted back to the image space.

1) Human brain SPECT: In Fig. 11(a), the left column shows, from top to bottom, the SRF maps of three representative scintillators on the inner, middle and outer detector layers respectively. Each SRF is accompanied by a zoom-in view of a 20 mm × 20 mm region marked in the corresponding SRF map. The section profiles in the right column correspond to the segment indicated in the zoom-in view SRF maps on the same row. The SRFs on different layers of scintillators are similar in shape but have different sensitivity. We observe that 1) a scintillator on any layer of a MATRICES module collects photons from multiple stripe-shaped regions, created by apertures on the metal plate and the passages formed by the scintillators in front of it; and 2) progressing from inner to outer layer, the absolute pixel sensitivity decreases, as is represented by the maximum value shown above the palette
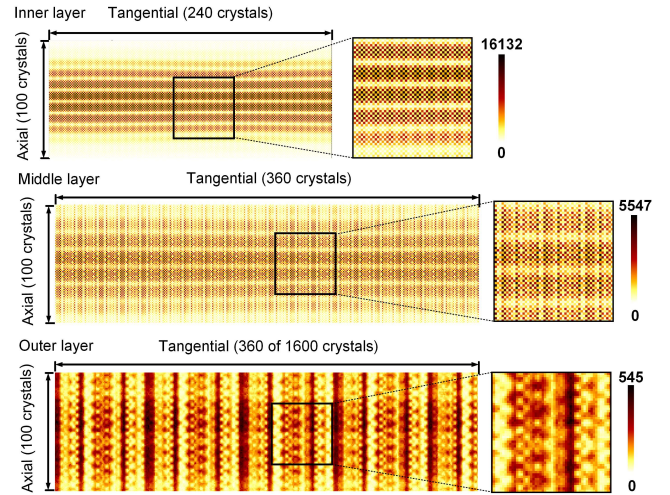

Fig. 10. Projection images of a 5 mm (∅) × 3 mm (L) cylindrical source on the simulated mouse SPECT. Full images on the inner and middle layer crystals are shown in the top and middle rows, respectively. A partial outer-layer projection image is shown in the bottom row. A zoom-in view on a segment of each image is shown for better visualization of details.

bar; whilst the sensitive stripes are confined more narrowly, which implies higher spatial resolution. This is the result of having increased number of collimating layer(s) in-between the object and the detector layer.

2) Mouse SPECT: Similar to Fig. 11, III-C shows the SRFs of three scintillators on the inner, middle and outer layer detectors respectively of the mouse SPECT system. In III-C, the sensitive stripes are narrower as a result of using narrower scintillators in MATRICES.

Interestingly, we find that the stripe profile of an outer-layer scintillator, as shown in Fig. 11(b) and III-C(b), has an irregular shape. This is interpreted by the fact that in the MATRICES structure, the inner- and middle- layer scintillators absorb only a portion of photons in each channel. The different attenuation properties between neighboring scintillators cause non-uniform photon absorption and hence streaks in the SRF's stripes. The FWHM of a SRF stripe, i.e. 0.98 mm in Fig. 11(b) and 350 μm in III-C(b), is significantly smaller than the width of the crystal and the collimator hole, i.e 2 mm in the brain SPECT and 1 mm in the mouse SPECT respectively. This implies a higher resolution beyond the limit of the geometrical width of the crystals and metal apertures.

3) Prototype SPECT: The SRFs of three representative scintillators in the prototype SPECT are shown in Fig. 13. Since the SRFs are measured in a 1.35 mm × 1.35 mm FOV (see Section II.E.3)), only one stripe appears in each of the SRFs, and the SRF shown in Fig. 13 (a) is incomplete. Outer layer scintillators acquire less events, and show narrower SRF than the inner layer scintillators, this confirms the findings in the simulations. The FWHM of the outer layer scintillator's SRF is also much smaller than the size of the scintillator and the size of apertures on the metal ring. The difference between measured SRFs in Fig. 13 and simulated counterparts in III-C are mainly caused by experimental factors,

(a) Inner layer crystal

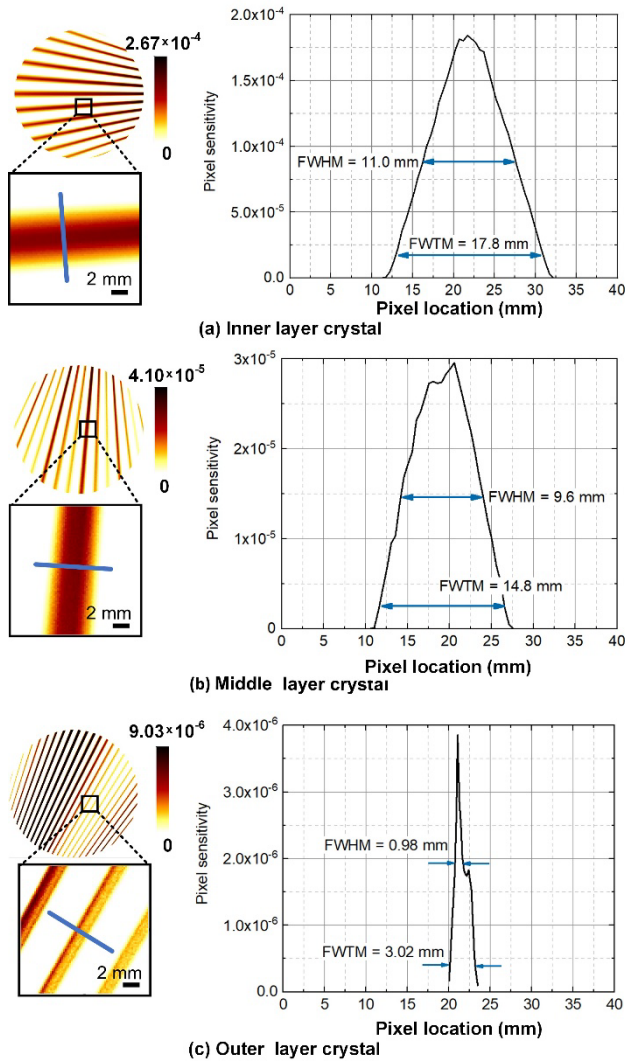**(b) Middle layer crystal**

(c) Outer layer crystal

Fig. 11. Sample SRFs for the human brain SPECT. From top to bottom, the SRFs of three scintillators on the inner, middle and outer detector layer respectively are shown in the left column. Each SRF is accompanied by a zoom-in view of a selected 20 mm × 20 mm region. The right column consists of section profiles of the SRFs on the left, with the section location marked by the blue line-segment in the zoom-in view.

(a) Inner layer

(b) Middle layer

(c) Outer layer

Fig. 12. Sample SRFs for the mouse SPECT. It uses the same figure arrangements as in Fig. 11.

including limited FOV, different scintillator size, the 300 μm diameter of the point source used in matrix measurement, as well as the background subtraction step in experimental data processing.

The SRF analysis of the above 3 systems shows that the MATRICES architecture integrates high resolution (in outer layers) and high sensitivity detectors (in inner layers) in one system. That foretells a superb performance of the MATRICES.

C. Resolution

1) Human Brain SPECT: The resolution performance is demonstrated in Fig. 14 with hot rod phantom images. At the four count levels evaluated, the smallest visible hot rods are 0.5 mm, 0.75 mm, 1.0 mm and 1.2 mm respectively.

2) Simulated Mouse SPECT: Fig. 15 shows the hot-rod phantom images at 3 count levels. The respective smallest
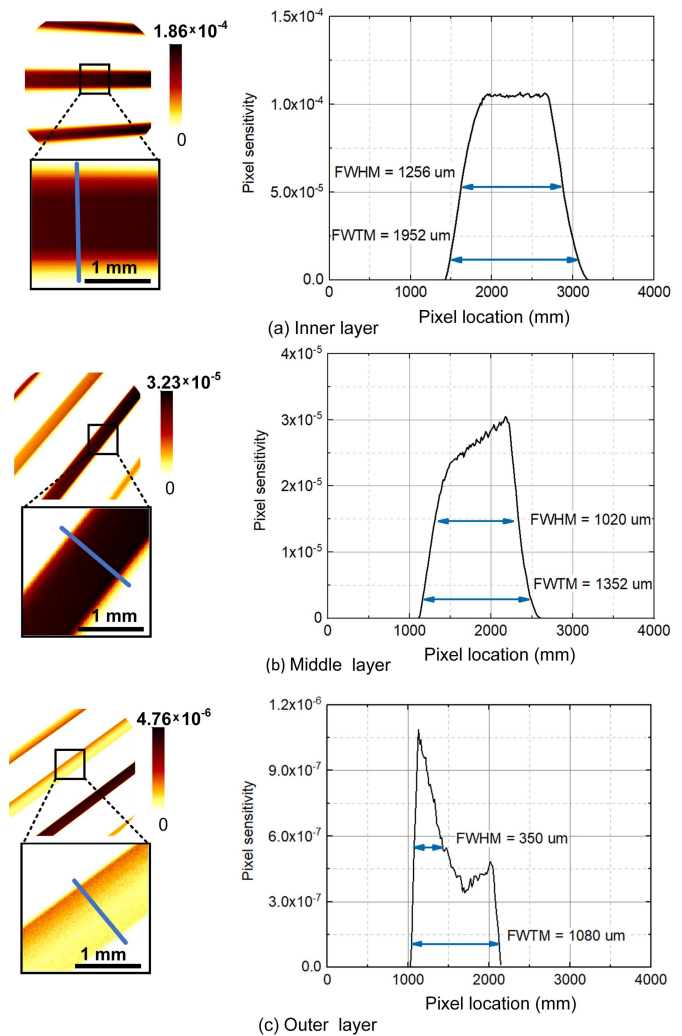
hot-rod diameters of the resolvable sections are 50, 80 and 100 μm.

3) Prototype SPECT: One representative trans-axial image from each of the three point-source phantoms is shown in Fig. 16. The point sources are clearly resolved in the 0.6-mm and 0.45-mm grid-step phantom images, and still visually separable in the 0.3-mm grid-step phantom image.

The reconstructed images of the 0.3-mm grid-step point-source phantom centered at six different locations in the FOV are shown in Fig. 17. The point sources are visually separable in all the images. The clarity of the images degrades with reduced acquisition time, but even at 7.5 min, the point sources are mostly separable in trans-axial planes (Slices A and B). The images appear less clear in coronal and sagittal slices (Slices C and D), this is likely due to the larger scintillator size in the axial direction. At the edge of (Fig. 17 (f)) or even outside (Fig. 17(g)) the 10 mm × 10 mm × 10 mm FOV, the image resolution is slightly better. Further studies are ongoing to fully characterize the performance of the prototype system.
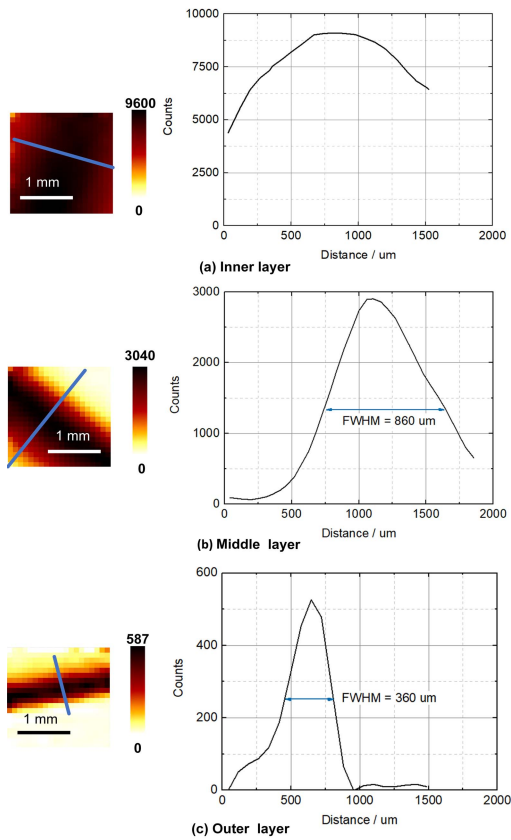
Fig. 13. Sample SRFs for the experimental prototype SPECT. Left column: From top to bottom, the SRFs of three scintillators on the inner, middle and outer detector layers respectively. Right column: Sample section profiles of the SRFs on the left. The position of each section is marked in the SRF image.

D. Contrast to Noise Ratio (CNR)

1) Brain SPECT: The CNR results of the two contrast phantom studies are shown in Fig. 18. For each study, 4 graphs — each for one acquisition time — are presented, each graph reports the CNRs of the hot-rods of 6 sizes as a function of reconstruction iteration number. As expected, shorter acquisitions yield lower CNR curves. All CNR curves reach a maximum at certain early iterations and start to decline due to the increase of noise in the warm background region as iteration number increases.

When the contrast phantom is placed in air (Fig. 18 (a)-(d)), the diameters of the smallest visible (with a criteria of highest achieved CNR over all iterations > 5.0) hot rods are 1.0 mm (at 120 iterations), 1.0 mm (at 62 iterations), 2.0 mm (at 8 iterations), and 2.5 mm (at 4 iterations) respectively for studies correspond to the four acquisition times. When the phantom is placed in water (Fig. 18 (e)-(h)), the CNR values slightly decrease in most cases. In certain cases (e.g. comparing (a) to (e) and (b) to (f)), the CNR values with the water phantom is higher. This is due to the inaccurately higher contrast (which is higher than the 5:1 true activity ratio) measured from the reconstructed image. We believe this is caused by photon attenuation and scattering. The diameters of the smallest visible hot rods are still 1.0 mm (at 119 iterations), 1.0 mm (at 61 iterations), 2.0 mm (at 14 iterations) and 2.5 mm (at 4 iterations).
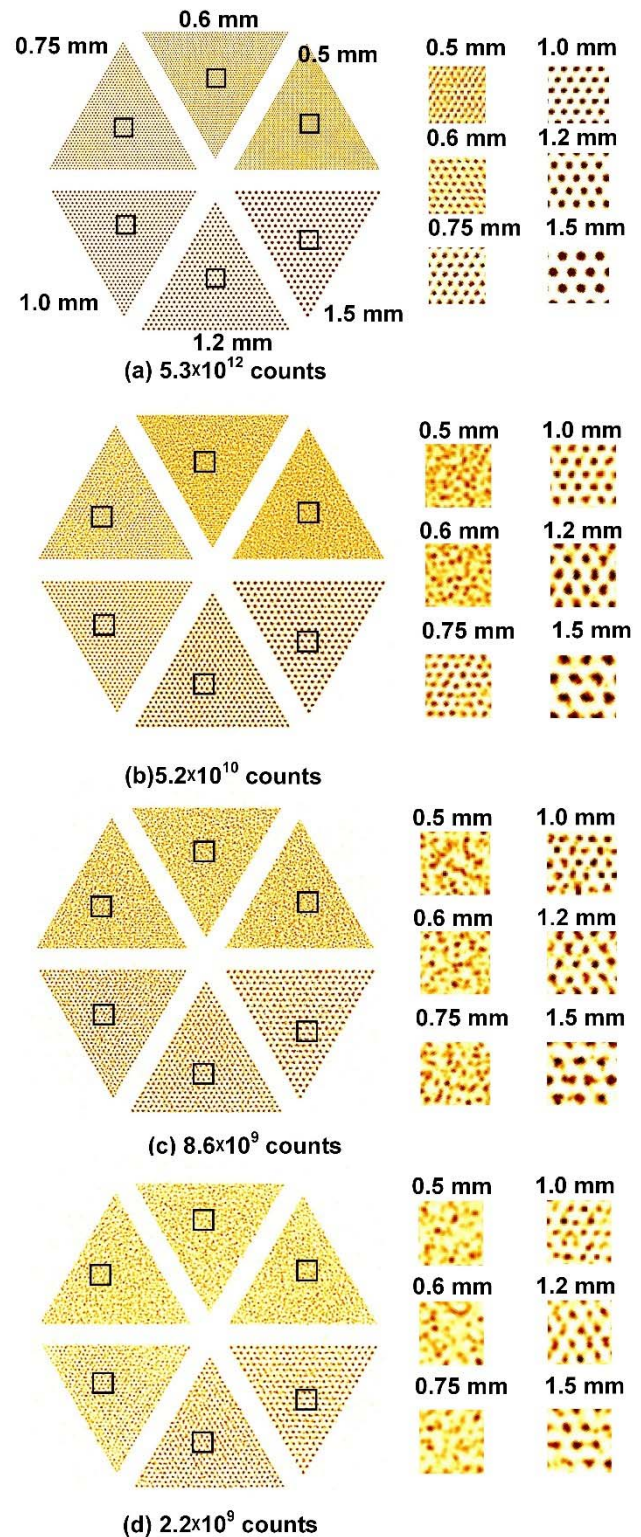

Fig. 14. Reconstructed images of the planar hot rod phantom acquired in four count-levels on the brain SPECT. A zoom-in view of a small area in each hot-rod pattern sections is shown on the right side of each image.

For each graph in Fig. 18, the corresponding reconstructed image at the iteration when the highest CNR of the smallest visible hot rod (CNR > 5) is achieved is shown in Fig. 19. The images confirm the indication of the CNR values.

(a) 2.2×10¹² counts

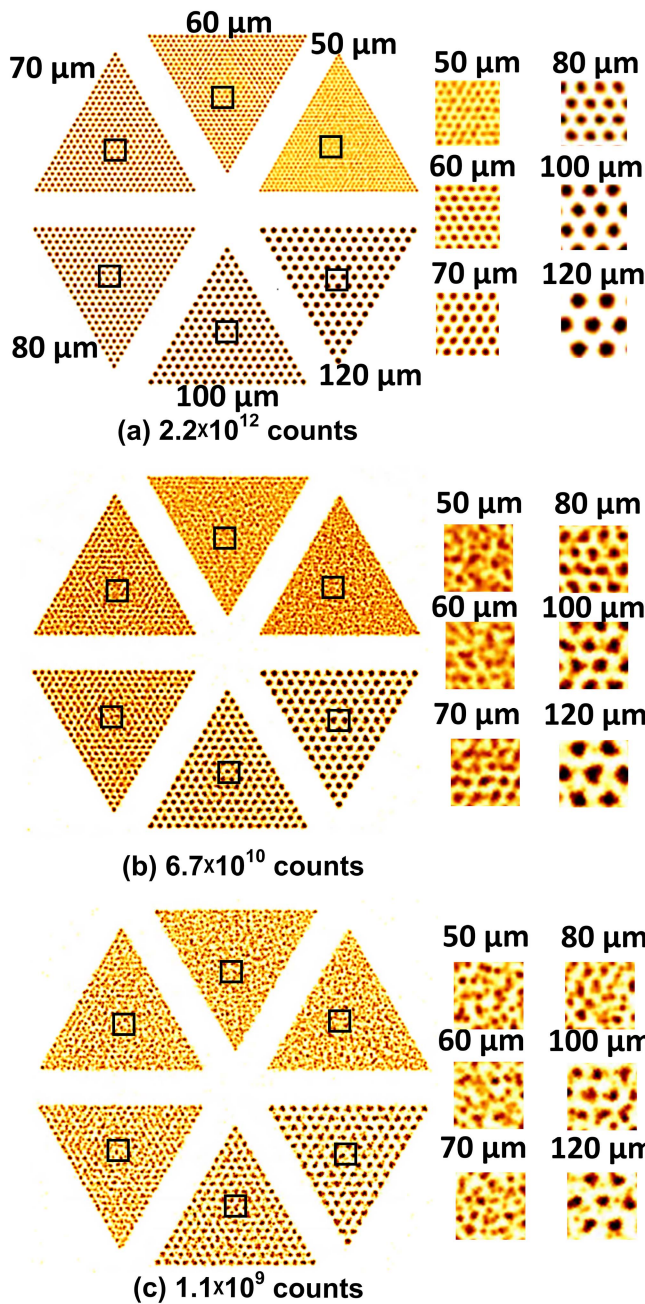**(b) 6.7×10¹⁰ counts**

(c) 1.1×10⁹ counts

Fig. 15.   Reconstructed images of the hot rod phantom for the animal self-collimating SPECT at statistical noise levels. A zoom-in view of a small area in each hot-rod pattern sections is shown on the right side of each image.
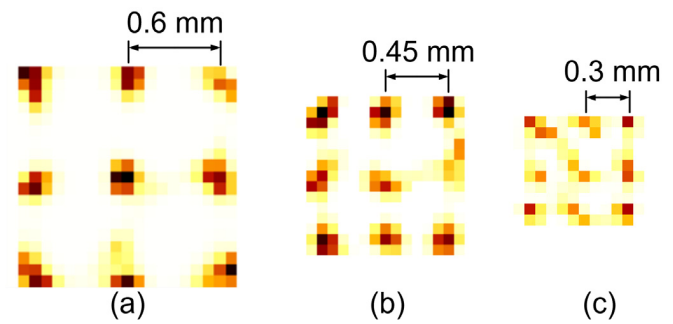

Fig. 16.   Representative trans-axial view images of the three point-source phantoms. The center-to-center distances between neighboring point sources are labeled in each image. The diameter of all the point sources is 0.3 mm.

Consistent with that observed in the CNR graphs in Fig. 18, the image qualities appear slightly degraded when the contrast phantom is immersed in water.

2) Simulated Mouse SPECT: The CNR *vs.* iteration curves of the contrast phantom studies for the mouse SPECT are shown in Fig. 20. With a criterion of highest CNR > 5.0, the diameters of the smallest visible hot rods are 0.14 (at 73 iterations), 0.20 (at 39 iterations), 0.25 (at 8 iterations) and 0.30 mm (at 6 iterations) for studies correspond to the acquisition times 20 hr, 7.5 hr, 1 hr and 20 min, respectively. The corresponding reconstructed image at the iteration when

the highest CNR of the smallest visible hot rod is achieved, is shown in Fig. 21.

Comparing Fig. 21 with the contrast phantom images for the brain SPECT (Fig. 19), we observe ring artifacts in trans-axial slices in Fig. 19, but there are no such artifacts in Fig. 21. We believe this is because that the number of voxels in these simulations are similar (150,000 for the brain SPECT vs 163,840 for the mouse SPECT, but the number of detectors for the brain SPECT (247,680) is much less than that for the mouse SPECT (660,000), as is listed in Table IV. Therefore, the reconstructions for the brain SPECT may be more unstable, i.e. increased uncertainty. Since the system has a ring-shaped symmetric geometry, the uncertainty may likely be expressed as the ring-artifacts.

IV. DISCUSSION

A. Self-Collimation Concept

In this work we introduce a novel detector architecture MATRICES and the self-collimation concept for improving SPECT imaging performance. The essential element of the new concept is to let sensitive detectors also play the role of collimators, as illustrated in Fig. 1(c). Unlike conventional mechanical collimators, self-collimation does not impose a complete interdependency between the imaging system's spatial resolution and sensitivity performance, therefore breaks away from the conventional SPECT technology. Monte Carlo simulations and experimental studies with three SPECT system configurations demonstrate clearly the significant advantages of this approach.

B. Choices of Mosaic Scintillators

While we choose to start the investigation of the MATRICES with scintillator-pairs of strong contrast of linear attenuation coefficients, there is a wealth of scintillator combinations to be explored. It is impractical to assemble several real systems with different scintillator combinations, but it is also important to show that the concept can be implemented with a variety of practically available scintillators. Therefore, we decide to test one combination on the prototype and study two other combinations on the simulated systems.

Besides using contrast scintillator pairs, there are also other ways to enable the collimation function in the inner and
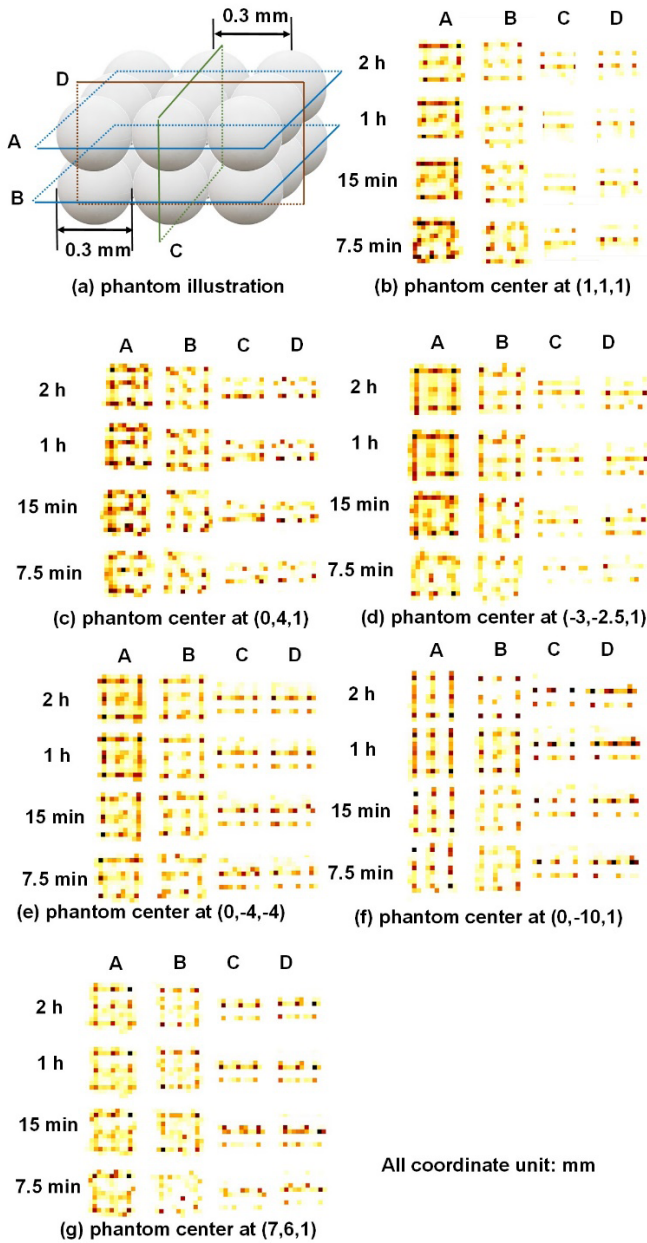
Fig. 17. (a) Illustration of the 0.3-mm grid-step point-source phantom imaged on the prototype, and the locations of the image slices A, B, C and D. Each image-set in (b)–(f) corresponds to a study of the phantom centered at a unique location. In an image-set, the row-label indicates the acquisition time or statistics level of acquired events, the column-label indicates the slice-location of the images in the column.
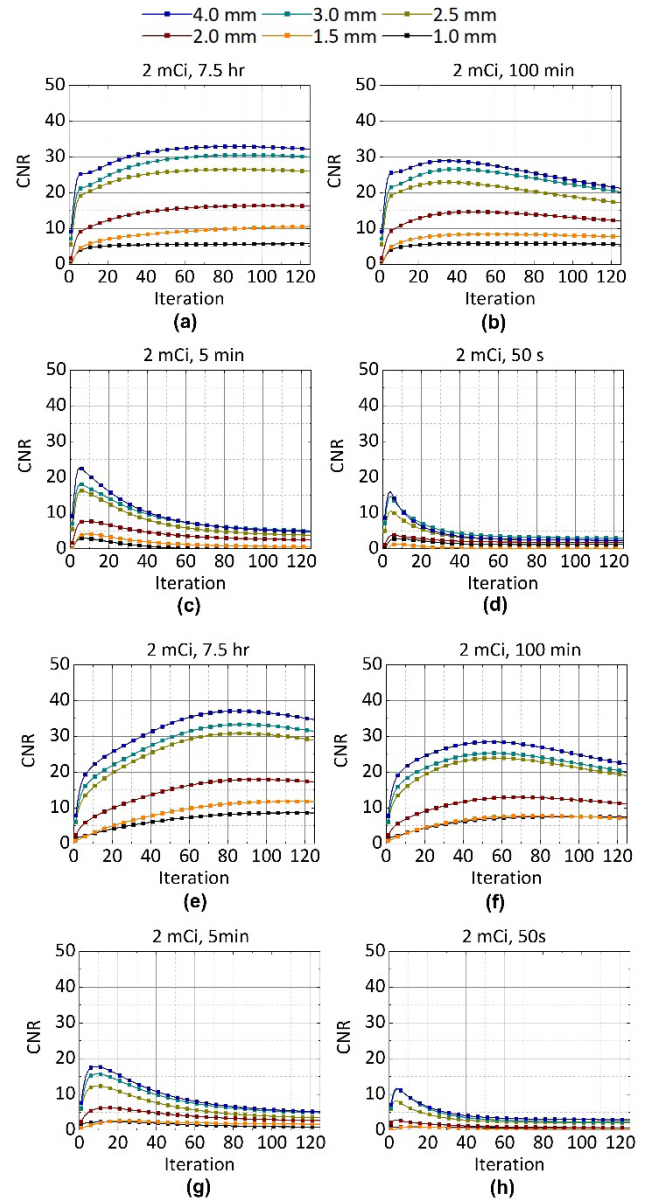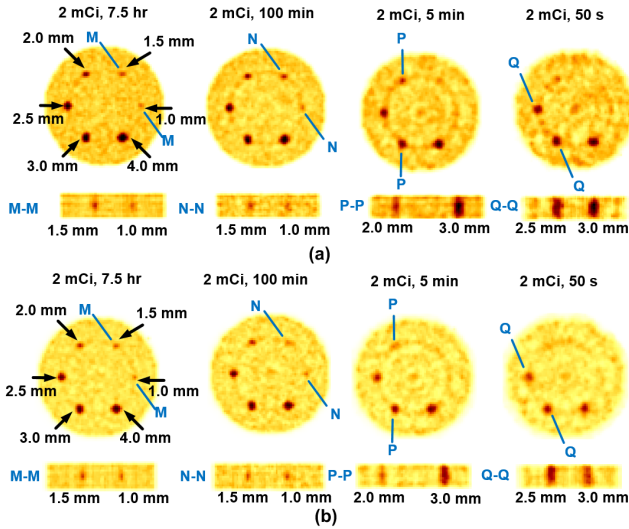

Fig. 18. CNR results of the contrast phantom for the brain SPECT. Graphs from (a) to (d) are phantom-in-air results, from (e) to (h) are phantom-in-water results. Each graph consists of CNRs of the hot-rods as a function of reconstruction iteration number.

detector assembling. A different event processing logic is also required to deal with crystal scattering events that produce multiple signals on adjacent crystals.
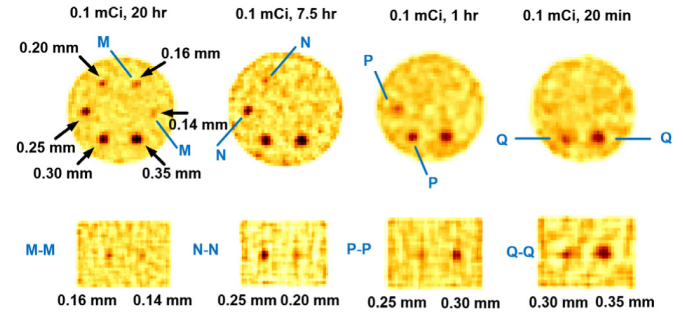
C. Challenges and Opportunities in Configuration Optimization

It should be noted that the approach in Section II.D does not guarantee a global optimization of the parameter set $\{r, D_2, D_3, t_2, t_3\}$. Considering the complicated geometry of a MATRICES SPECT system and the long computational time for matrix inverse, it is extremely hard to find the global optimal solution within the realistic time. On the other hand, the focus of this work is to demonstrate the system

middle layers, e.g. assembling the detector with one type of small sized crystal and allowing a certain gap between neighboring crystals (or crystal blocks). This design would likely lead to a new balance between collimation and photon detection functions on inner and middle layer detectors, but a complete study on this subject is out of the scope of this work. Our current available detector block fabrication and readout electronics technologies are designed to solely support building continuous detector blocks. Having large gaps in between crystals (or crystal blocks) brings challenges to

Fig. 19. Images of the 3-D contrast phantom reconstructed with the iteration number that achieves the highest CNR of the smallest visible hot rod (CNR > 5.0). (a) Phantom in air. Top-row: transverse view. Bottom row: Vertical cross-section views marked by M-M, N-N, P-P and Q-Q for examining the smallest visible hot rod. All images use the same color scale. (b) Phantom in water. Other display arrangements are the same as in (a).
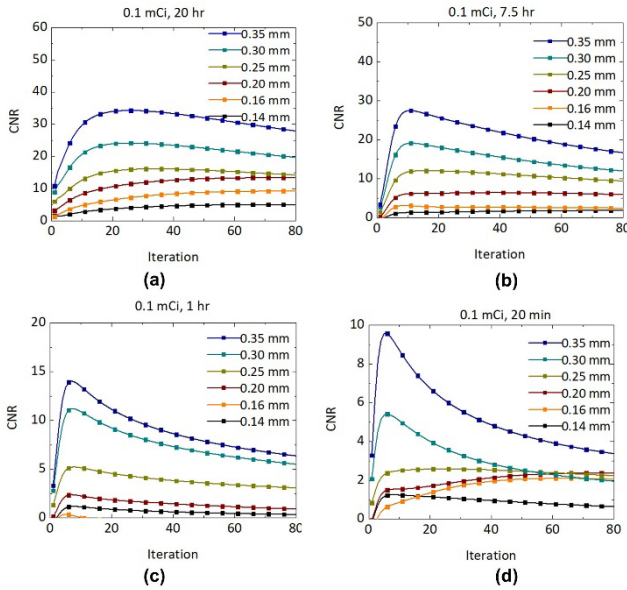

Fig. 20. CNR results of the contrast phantom for the mouse SPECT. Each graph consists of CNRs of the hot-rods of different sizes as a function of reconstruction iteration number.

performance of a MATRICES system, rather than optimizing all the parameters.

Our current optimizations are also limited to only the in-plane parameters due to following reasons: 1) The extensive computational time of the multi-ray-tracing calculation of A; 2) The huge computer memory requirement in calculating matrix inverse $[\text{diag}(A\theta)]^{-1}$ and $(I + \lambda F)^{-1}$. To run the optimization in a 3-D system is impractical with our available computational resources. Therefore, similar to [42], we extend the geometrical setup on the 2-D metal ring to a 3-D metal plate.

Fig. 21. Images of the 3-D contrast phantom at 4 count levels reconstructed at the iteration when the highest CNR of the smallest visible hot rod (CNR > 5.0) is achieved. Top row: Transverse view. Bottom row: Vertical cross-section views marked by M-M, N-N, P-P and Q-Q for examining the smallest visible hot rod.

While the evaluations presented already show promising results, much further work is still required to fully understand the complicated relationship between the detector properties and system performance in a self-collimating SPECT system. For the outer layer in a MATRICES structure, the desired detector requirement is straightforward, i.e. high stopping power, high energy resolution, and small crystal size. For inner and middle layers, a high energy resolution is also desired. But for those parameters that impact the trade-off of collimation / detection functions, e.g. stopping power, crystal size, and the position of each layer, one cannot simply tell that tuning a certain parameter toward one direction would simply lead to monotonic system performance change. Looking from a different point-of-view, the MATRICES architecture provides plenty of opportunities for further development and optimization. The geometrical parameters of the metal layer and the apertures, the number and geometry of detector layers, the dimensions and materials of the scintillators on each detector layer, the functional balance of collimation and detection on each layer, or invention of other architectures that implements self-collimation, would create an intriguing and challenging system optimization task for researchers in the emission tomography community to solve. Researches on those topics would further enrich the imaging theory and technique of emission tomography.

D. Scintillator Size

In our simulation studies, the cross-sectional sizes of scintillators are chosen in accordance with state-of-art detector technologies in nuclear medicine imaging systems. Considering that the ring-shaped system design shown in Fig. 2(b) are similar to a PET system, we use the knowledge of modern PET detector technologies to determine the scintillator design. In the brain SPECT, we choose a 2 mm × 2 mm crystal size, which is close to the 2.1 mm × 2.1 mm crystal size in the HRRT brain PET system [43]. In the mouse SPECT, we choose a 1 mm × 1 mm crystal size, which is known to be decodable with state-of-art PET detector technology [44]. In the prototype, though we plan to match the system design to the simulated mouse SPECT, the crystal size at the present version is limited by the available detector technology support

in our lab, which is 1.35 mm × 2.7 mm (See Section II.D.3) for details).

E. What Enables the High Resolution

While the significantly reduced mechanical collimator leads to the overall sensitivity increase of the detector system, the very high resolution we demonstrate is considered to be the combined effect of the MATRICES architecture and additional sampling through the rotational movements of the aperture metal ring and translational movements of the object. The photon events collected on the outer layer detectors in MATRICES contains high resolution information. Although the counts of these events are much less than the low-resolution events collected on the inner and middle layer detectors, it appears the high-resolution events play a dominate role in achieving the resolution performance of the system. A separate preliminary study we conduct shows that the events from different detector layers all contribute, although differently in terms of their resolution property and statistical quantity, towards improving the image quality. This finding is consistent with the image resolution and SNR improvement reported on virtual pinhole PET [36], [45] and zoom-in PET [37] when events with variable resolution properties are involved.

The approach to use translational movements of the phantom to improve spatial sampling has been applied in other conventional SPECT systems [40], [46]. In this super high resolution self-collimating SPECT, the translational movements play an important role. Since improving the resolution means an increasing number of (and smaller) image voxels need to be sufficiently sampled with the same number of detectors, the translational move of the phantom effectively addresses this challenge by allowing each detector to "see" a different voxel at each move. However, using more movement steps means less count acquired in projection at each step and hence induces trade-off between resolution and noise.

Although our empirical demonstration through simulations and experiment is convincing and encouraging, the complex shape of the SRF in a self-collimating SPECT, as shown in Fig. 11-12, implies there is a strong need for a fundamental study to characterize the impact of the irregular shape of SRFs and reveal the optimal strategy of spatial sampling. Such a study may be still stemmed from established methods in conventional collimator and scanning protocol design approach [40].

F. Prototype Mouse System's Performance

The prototype mouse system reports clearly a lower resolution and sensitivity than its simulated counterpart. We attribute this to the sub-optimal size of the point sources used and several mismatched components between the prototype and simulated systems.

The smallest point source we can make in our lab is 0.3 mm in diameter. It is too big, in a conventional hot-rod phantom configuration, to demonstrate the resolution level achieved on the simulated mouse SPECT. But with the unconventional point source phantoms we design, i.e. one with 0.45-mm and the other 0.3-mm grid-step as shown in Fig. 16, we show

the imaging resolution of the prototype should be much better than 0.3 mm. The 0.3-mm center-to-center distance between neighboring point-sources means the neighboring point sources actually touch each other on the edge, as illustrated in Fig. 17 (a). The fact that these point sources are still separable in the images (Fig. 17) indicates that the reduction of activity in the voxels near the intersection point of two neighboring point sources is preserved in the imaging process. In other words, the imaging system's resolution must be much better than 0.3 mm. This conclusion also indicates that using 0.3-mm diameter point source for system matrix measurement does not introduce significant resolution degradation.

The sensitivity discrepancy between the prototype and simulated SPECT may be the result of four mismatched components between the two systems. First, the axial length of the detector module on the prototype is 65 mm, whereas it is 100 mm on the simulated system. Second, the prototype uses a heptagonal geometry. The physical package of the detector modules and implementation create considerable between-detector-module gaps which do not exist on the simulated system. Third, each detector module on the prototype presents a 2-mm thick tungsten shielding on the sides of each detector module (which is not required in a full-ring scanner). The shielding absorbs a large portion of the oblique photons but is not included in the simulated system. Fourth, the readout electronics on the inner and middle layer detectors on the prototype absorbs an estimated 10% to 20% of photons at 140 keV and are not included on the simulated system. We expect that the optimization of these factors, for example, minimizing the detector-module side-shielding, will bring the performance of the protype system close to that of its simulated counterpart.

The prototype's imaging volume presented in this study is only 10 mm × 10 mm × 10 mm, due to the time-consuming process for system matrix measurement. We expect that the actual FOV of the prototype to be close to that confined by the metal ring diameter, 38 mm, and the axial height, 65 mm, of the prototype. We are continuing the system matrix measurements to increase the FOV in the future.

G. Positron Emitting Nuclides

The MATRICES self-collimating architecture may be further improved for positron emitting tracers. The inner aperture metal layer can then be replaced by sensitive detectors equipped with the coincidence detection of annihilation photons. This shall further improve the system sensitivity. The multiple layer structure of MATRICES shall also mitigate the depth-of-interaction effect of the high energy annihilation photons.

H. Multiplexing

Unlike that of a conventional mechanical collimator based SPECT, the SRFs of individual scintillators in Fig. 11 and III-C show a shape of multiple stripes, which indicates that photons coming from the voxels in each stripe are multiplexed on the scintillator. However, as shown in Section III.C, unlike other multiplexing work [47] in literature, excellent resolution and signal-to-noise ratio performance are simultaneously

achieved in both brain and mouse SPECT. A full study on this topic would further reveal the comprehensive contribution of various factors to the image quality, including the improvement of spatial resolution and sensitivity and the information loss due to multiplexing.

The higher sensitivity of self-collimation comes from reduced mechanical collimation (absorption) rather than multiplexing. The coded-aperture collimation, as the extreme of multiplexed multi-pinhole collimation, is known for increasing the sensitivity but suffers from significant ambiguity. It achieves high spatial resolution through magnification similar to that of pinhole collimation, but fails to provide higher signal-to-noise ratio when the image object is not sparse [5]. In comparison, the self-collimation approach separates the detector into multiple layers, events reaching the middle and outer layer detectors are collimated by sensitive detectors and through combined photon pathways. Such approach both efficiently alleviates the impact of multiplexing and improves spatial resolution than the pinhole induced magnification effect. On the other hand, the Compton gamma camera [48], [49] also employs two or more separate detector layers. Its sensitivity is limited by the requirement that the primary photon must be scattered in the scattering layer(s), and the scattered photon must be absorbed in the absorbing layer(s). Its spatial resolution is limited by the cone-shaped SRF, and more importantly, the further blurring of the SRF due to Doppler broadening effect and energy measurement uncertainties. The latter factor is even more challenging for imaging 140 keV photons for ^{99m}Tc SPECT due to the critical requirement of both high energy resolution and good Compton scattering cross section. The application of Compton scattering collimation to SPECT imaging achieves several millimeters to over one centimeter spatial resolution, and less than 0.1% sensitivity [50]. In comparison, a self-collimating SPECT has much less critical requirement to the energy resolution of detector materials, and could have one order-of-magnitude higher spatial resolution and sensitivity according to our study.

I. Photon Energy Range

For a self-collimating SPECT, the energy of the gamma ray source impacts the system performance in a different way than for a conventional SPECT. Our current system design is made for 140 keV photons emitted from ^{99m}Tc labeled tracers (which cover ~85% of tracer uses in diagnostic SPECT imaging), but the MATRICES architecture and the self-collimating concept are suitable in principle for high energy gamma photons including 511 keV annihilation photons from PET tracers. Being able to image a broad range of gamma photons also allows imaging of multiple tracers simultaneously with energy-based separation methods, which provides the opportunity to study the dynamics of multiple competing biological processes.

For tracers with other photon energies, the photon penetration behavior on the metal layer, and more importantly, the collimation and detection functions on each detector layer may vary. One possible way to compensate for the energy change might be tuning the thickness of detector layers

accordingly so that photon absorption portion in each layer remains the same. However, further validation studies are required, considering that both detectors' thickness and width will impact the probability of photon absorption when photons come from all directions. The impact of detector scattering should also be considered. Optimal design of other detector layouts, including detector materials, arrangement of different crystals to assemble the mosaic detector, and ring diameters of each layer, are also energy dependent and yet to be revealed. Complete system optimization studies for isotopes other than ^{99m}Tc are planned in the future.

It is also worth noting that in our simulations, the 120 – 160 energy window setup causes 12.7% and 14.2% photon loss due to detector scattering on the brain SPECT using GSO/YSO scintillators and mouse SPECT using GAGG(Ce)/YSO scintillators respectively. In our proof-of-concept study, we use non-hygroscopic scintillators that have lower energy resolution than NaI(Tl). It is possible in the future to employ NaI(Tl) or other high-energy-resolution detector materials in industrial practice. What's more, similar to the Compton-PET concept in [51], further sensitivity improvement without losing detector intrinsic resolution is possible in the MATRICES detector system by allowing coincidence detection of multiple interactions on each individual detectors.

V. CONCLUSION

In this work, we introduce a self-collimation concept and a MATRICES architecture for simultaneously improving the spatial resolution and sensitivity of SPECT imaging. Three MATRICES SPECT systems are designed and evaluated. The simulated human brain SPECT achieves 3.88% sensitivity, it clearly resolves 0.5-mm and 1.0-mm hot-rod patterns at noise-free and realistic count-levels, respectively; The simulated mouse SPECT achieves 1.25% sensitivity, it clearly resolves 50-μm and 100-μm hot-rod patterns at noise-free and realistic count-levels, respectively; the SPECT prototype achieves 0.14% sensitivity and clearly separates 0.3-mm-diameter point sources of which the center-to-center neighbor distance is also 0.3 mm. The superb performance indicates a potential paradigm shift in SPECT technology development. Given the rich selections of SPECT tracers, along with their long half-lives and well-established manufacturing and distribution infrastructure, it is reasonable to expect a strong emergence of self-collimating SPECT systems and a renaissance of SPECT applications.

REFERENCES

[1] S. R. Meikle, P. Kench, M. Kassiou, and R. B. Banati, "Small animal SPECT and its place in the matrix of molecular imaging technologies," *Phys. Med. Biol.*, vol. 50, no. 22, pp. R45–R61, Nov. 2005, doi: 10.1088/0031-9155/50/22/r01.

[2] M. Baker, "The whole picture," *Nature*, vol. 463, no. 7283, p. 977, Feb. 2010, doi: 10.1038/463977a.

[3] H. O. Anger, "Scintillation camera with multichannel collimators," *J. Nucl. Med.*, vol. 5, no. 7, pp. 515–531, 1964. [Online]. Available: http://jnm.snmjournals.org/content/5/7/515.short

[4] S. Moore, K. Kouris, and I. Cullum, "Collimator design for single photon emission tomography," *Eur. J. Nucl. Med.*, vol. 19, no. 2, pp. 138–150, Feb. 1992, doi: 10.1007/BF00184130.

[5] K. Van Audenhaege, R. Van Holen, S. Vandenberghe, C. Vanhove, S. D. Metzler, and S. C. Moore, "Review of SPECT collimator selection, optimization, and fabrication for clinical and preclinical imaging," *Med. Phys.*, vol. 42, no. 8, pp. 4796–4813, Jul. 2015, doi: 10.1118/1.4927061.

[6] F. Beekman and F. van der Have, "The pinhole: Gateway to ultra-high-resolution three-dimensional radionuclide imaging," *Eur. J. Nucl. Med. Mol. Imag.*, vol. 34, no. 2, pp. 151–161, Feb. 2007, doi: 10.1007/s00259-006-0248-6.

[7] S. Wang, T. Ma, and R. Yao, "Axial movement parameter study on preclinical slit-slat SPECT," *IEEE Trans. Nucl. Sci.*, vol. 63, no. 1, pp. 84–89, Feb. 2016, doi: 10.1109/tns.2015.2493043.

[8] J. Strologas, M. Rozler, S. Metzler, D. Stentz, S. Poopalasingam, and W. Chang, "C-SPECT, a novel cardiac single-photon emission computed tomography system," in *Proc. 38th Int. Conf. High Energy Phys. PoS(ICHEP)*, vol. 282, Feb. 2017, p. 869.

[9] S. T. Mahmood, K. Erlandsson, I. Cullum, and B. F. Hutton, "Design of a novel slit-slat collimator system for SPECT imaging of the human brain," *Phys. Med. Biol.*, vol. 54, no. 11, pp. 3433–3449, Jun. 2009, doi: 10.1088/0031-9155/54/11/011.

[10] S. Sajedi *et al.*, "Design and development of a high resolution animal SPECT scanner dedicated for rat and mouse imaging," *Nucl. Instrum. Methods Phys. Res. A, Accel. Spectrom. Detect. Assoc. Equip.*, vol. 741, pp. 169–176, Mar. 2014, doi: 10.1016/j.nima.2014.01.001.

[11] L. Imbert *et al.*, "Compared performance of high-sensitivity cameras dedicated to myocardial perfusion SPECT: A comprehensive analysis of phantom and human images," *J. Nucl. Med.*, vol. 53, no. 12, pp. 1897–1903, Dec. 2012. [Online]. Available: http://jnm.snmjournals.org/content/ 53/12/1897.abstract

[12] M. A. King, J. M. Mukherjee, A. Konik, I. G. Zubal, J. Dey, and R. Licho, "Design of a multi-pinhole collimator for I-123 DaTscan imaging on dual-headed SPECT systems in combination with a fan-beam collimator," *IEEE Trans. Nucl. Sci.*, vol. 63, no. 1, pp. 90–97, Feb. 2016, doi: 10.1109/TNS.2515519.

[13] O. Ivashchenko *et al.*, "Quarter-millimeter-resolution molecular mouse imaging with U-SPECT$^+$," *Mol. Imag.*, vol. 14, no. 1, p. 7290, Jan. 2015, doi: 10.2310/7290.2014.00053.

[14] M. Bocher, I. M. Blevis, L. Tsukerman, Y. Shrem, G. Kovalski, and L. Volokh, "A fast cardiac gamma camera with dynamic SPECT capabilities: Design, system validation and future potential," *Eur. J. Nucl. Med. Mol. Imag.*, vol. 37, no. 10, pp. 1887–1902, Oct. 2010, doi: 10.1007/s00259-010-1488-z.

[15] F. Beekman *et al.*, "G-SPECT-I: A full ring high sensitivity and ultra-fast clinical molecular imaging system with <3 mm resolution," *Eur. J. Nucl. Med. Mol. Imag.*, vol. 42, p. S209, Mar. 2015.

[16] Y. Chen, B. Vastenhouw, C. Wu, M. C. Goorden, and F. J. Beekman, "Optimized image acquisition for dopamine transporter imaging with ultra-high resolution clinical pinhole SPECT," *Phys. Med. Biol.*, vol. 63, no. 22, Nov. 2018, Art. no. 225002, doi: 10.1088/1361-6560/aae76c.

[17] S. R. Meikle, R. R. Fulton, S. Eberl, M. Dahlbom, K.-P. Wong, and M. J. Fulham, "An investigation of coded aperture imaging for small animal SPECT," *IEEE Trans. Nucl. Sci.*, vol. 48, no. 3, pp. 816–821, Jun. 2001.

[18] S. Jan *et al.*, "GATE: A simulation toolkit for PET and SPECT," *Phys. Med. Biol.*, vol. 49, no. 19, pp. 4543–4561, Oct. 2004, doi: 10.1088/0031-9155/49/19/007.

[19] R. Yao, T. Ma, and Y. Shao, "Lutetium oxyorthosilicate (LSO) intrinsic activity correction and minimal detectable target activity study for SPECT imaging with a LSO-based animal PET scanner," *Phys. Med. Biol.*, vol. 53, no. 16, pp. 4399–4415, Aug. 2008, doi: 10.1088/0031-9155/53/16/012.

[20] M. J. Berger. *XCOM: Photon Cross Sections Database*. Accessed: Apr. 20, 2021. [Online]. Available: https://physics.nist.gov/PhysRefData/Xcom/html/xcom1.html

[21] P. Lecoq, "Development of new scintillators for medical applications," *Nucl. Instrum. Methods Phys. Res. A, Accel. Spectrom. Detect. Assoc. Equip.*, vol. 809, pp. 130–139, Feb. 2016, doi: 10.1016/j.nima.2015.08.041.

[22] Q. Wei, N. Jiang, T. Xu, Z. Lyu, T. Ma, and Y. Liu, "A position sensitive scintillation detector using a side-by-side GAGG-F/GAGG-T phoswich block," *J. Instrum.*, vol. 15, no. 4, Apr. 2020, Art. no. T04001, doi: 10.1088/1748-0221/15/04/t04001.

[23] Q. Wei *et al.*, "A side-by-side LYSO/GAGG phoswich detector aiming for SPECT imaging," *Nucl. Instrum. Methods Phys. Res. A, Accel. Spectrom. Detect. Assoc. Equip.*, vol. 953, Feb. 2020, Art. no. 163242, doi: 10.1016/j.nima.2019.163242.

[24] N. Kudomi *et al.*, "Development of a GSO detector assembly for a continuous blood sampling system," *IEEE Trans. Nucl. Sci.*, vol. 50, no. 1, pp. 70–73, Feb. 2003, doi: 10.1109/TNS.2002.807869.

[25] S. Yamamoto, H. Watabe, Y. Kanai, K. Kato, and J. Hatazawa, "Development of a high-resolution YSO gamma camera system that employs 0.8-mm pixels," *Ann. Nucl. Med.*, vol. 28, no. 3, pp. 232–240, Apr. 2014, doi: 10.1007/s12149-013-0800-y.

[26] A. O. Hero, J. A. Fessler, and M. Usman, "Exploring estimator bias-variance tradeoffs using the uniform CR bound," *IEEE Trans. Signal Process.*, vol. 44, no. 8, pp. 2026–2041, 1996, doi: 10.1109/78.533723.

[27] N. H. Clinthorne *et al.*, "Theoretical performance comparison of a Compton-scatter aperture and parallel-hole collimator," in *Proc. IEEE Nucl. Sci. Symp. Conf. Rec.*, Nov. 1996, pp. 788–792, doi: 10.1109/NSS-MIC.1996.591443.

[28] L.-J. Meng and N. Li, "A vector uniform cramer-rao bound for SPECT system design," *IEEE Trans. Nucl. Sci.*, vol. 56, no. 1, pp. 81–90, Feb. 2009, doi: 10.1109/TNS.2008.2006609.

[29] N. Fuin, S. Pedemonte, S. Arridge, S. Ourselin, and B. F. Hutton, "Efficient determination of the uncertainty for the optimization of SPECT system design: A subsampled Fisher information matrix," *IEEE Trans. Med. Imag.*, vol. 33, no. 3, pp. 618–635, Mar. 2014, doi: 10.1109/TMI.2013.2292805.

[30] L. R. V. Pato, S. Vandenberghe, B. Vandeghinste, and R. Van Holen, "Evaluation of Fisher information matrix-based methods for fast assessment of image quality in pinhole SPECT," *IEEE Trans. Med. Imag.*, vol. 34, no. 9, pp. 1830–1842, Sep. 2015, doi: 10.1109/TMI.2015.2410342.

[31] Q. Wei *et al.*, "Crystal identification for a dual-layer-offset LYSO based PET system via Lu-176 background radiation and mean shift algorithm," *Phys. Med. Biol.*, vol. 63, no. 2, 2018, Art. no. 02NT01. [Online]. Available: http://stacks.iop.org/0031-9155/63/i=2/a=02NT01.

[32] T. Ma *et al.*, "Development of a SiPM based preclinical PET SPECT imaging system imaging system," *J. Nucl. Med.*, vol. 58, no. 1, p. 397, May 2017. [Online]. Available: http://jnm.snmjournals.org/content/58/supplement_1/397.abstract.

[33] Q. Wei, T. Ma, T. Xu, Y. Liu, S. Wang, and Y. Gu, "Evaluation of signal energy calculation methods for a light-sharing SiPM-based PET detector," *Nucl. Instrum. Methods Phys. Res. A, Accel. Spectrom. Detect. Assoc. Equip.*, vol. 848, pp. 81–86, Mar. 2017, doi: 10.1016/j.nima.2016.12.035.

[34] X. Zhu, Z. Deng, Y. Chen, Y. Liu, and Y. Liu, "Development of a 64-channel readout ASIC for an 8×8 SSPM array for PET and TOF-PET applications," *IEEE Trans. Nucl. Sci.*, vol. 63, no. 3, pp. 1327–1334, Mar. 2016, doi: 10.1109/TNS.2016.2518808.

[35] R. Yao, T. Ma, and Y. Shao, "Derivation of system matrix from simulation data for an animal SPECT with slit-slat collimator," *IEEE Trans. Nucl. Sci.*, vol. 56, no. 5, pp. 2651–2658, Oct. 2009, doi: 10.1109/TNS.2009.2022940.

[36] D. B. Keesing *et al.*, "Image reconstruction and system modeling techniques for virtual-pinhole PET insert systems," *Phys. Med. Biol.*, vol. 57, no. 9, pp. 2517–2538, May 2012, doi: 10.1088/0031-9155/57/9/2517.

[37] J. Zhou and J. Qi, "Adaptive imaging for lesion detection using a zoom-in PET system," *IEEE Trans. Med. Imag.*, vol. 30, no. 1, pp. 119–130, Jan. 2011, doi: 10.1109/TMI.2010.2064173.

[38] L. R. Furenlid *et al.*, "FastSPECT II: A second-generation high-resolution dynamic SPECT imager," *IEEE Trans. Nucl. Sci.*, vol. 51, no. 3, pp. 631–635, Jun. 2004, doi: 10.1109/TNS.2004.830975.

[39] C. Lackas, N. U. Schramm, J. W. Hoppin, U. Engeland, A. Wirrwar, and H. Halling, "T-SPECT: A novel imaging technique for small animal research," *IEEE Trans. Nucl. Sci.*, vol. 52, no. 1, pp. 181–187, Feb. 2005, doi: 10.1109/TNS.2005.843615.

[40] Y. Xia, R. Yao, X. Deng, Y. Liu, S. Wang, and T. Ma, "Assessment of hybrid rotation-translation scan schemes for in vivo animal SPECT imaging," *Phys. Med. Biol.*, vol. 58, no. 4, pp. 965–983, Feb. 2013, doi: 10.1088/0031-9155/58/4/965.

[41] H. M. Hudson and R. S. Larkin, "Accelerated image reconstruction using ordered subsets of projection data," *IEEE Trans. Med. Imag.*, vol. 13, no. 4, pp. 601–609, Dec. 1994, doi: 10.1109/42.363108.

[42] N. Fuin, A. Bousse, S. Pedemonte, S. Arridge, S. Ourselin, and B. Hutton, "Collimator design in SPECT, an optimisation tool," in *Proc. IEEE Nucl. Sci. Symp. Med. Imag. Conf.*, Oct. 2010, pp. 3149–3154, doi: 10.1109/NSSMIC.2010.5874382.

[43] H. W. A. M. D. Jong, F. H. P. V. Velden, R. W. Kloet, F. L. Buijs, R. Boellaard, and A. A. Lammertsma, "Performance evaluation of the ECAT HRRT: An LSO-LYSO double layer high resolution, high sensitivity scanner," *Phys. Med. Biol.*, vol. 52, no. 5, pp. 1505–1526, Mar. 2007, doi: 10.1088/0031-9155/52/5/019.

[44] Y.-C. Tai and R. Laforest, "Instrumentation aspects of animal PET," *Annu. Rev. Biomed. Eng.*, vol. 7, no. 1, pp. 255–285, Aug. 2005, doi: 10.1146/annurev.bioeng.6.040803.140021.

[45] J. Jiang *et al.*, "A second-generation virtual-pinhole PET device for enhancing contrast recovery and improving lesion detectability of a whole-body PET/CT scanner," *Med. Phys.*, vol. 46, no. 9, pp. 4165–4176, Sep. 2019, doi: 10.1002/mp.13724.

[46] N. Zeraatkar *et al.*, "Investigation of axial and angular sampling in multi-detector pinhole-SPECT brain imaging," *IEEE Trans. Med. Imag.*, vol. 39, no. 12, pp. 4209–4224, Dec. 2020, doi: 10.1109/TMI.2020.3015079.

[47] G. S. P. Mok, Y. Wang, and B. M. W. Tsui, "Quantification of the multiplexing effects in multi-pinhole small animal SPECT: A simulation study," *IEEE Trans. Nucl. Sci.*, vol. 56, no. 5, pp. 2636–2643, Oct. 2009, doi: 10.1109/TNS.2009.2023444.

[48] M. Fontana, D. Dauvergne, J. M. Létang, J.-L. Ley, and É. Testa, "Compton camera study for high efficiency SPECT and benchmark with anger system," *Phys. Med. Biol.*, vol. 62, no. 23, pp. 8794–8812, Nov. 2017, doi: 10.1088/1361-6560/aa926a.

[49] E. Muñoz *et al.*, "Performance evaluation of MACACO: A multilayer Compton camera," *Phys. Med. Biol.*, vol. 62, no. 18, pp. 7321–7341, Aug. 2017, doi: 10.1088/1361-6560/aa8070.

[50] M. Sakai *et al.*, "*In vivo* simultaneous imaging with 99mTc and 18F using a Compton camera," *Phys. Med. Biol.*, vol. 63, no. 20, Oct. 2018, p. 205006, doi: 10.1088/1361-6560/aae1d1.

[51] P. Peng, M. S. Judenhofer, and S. R. Cherry, "Compton PET: A layered structure PET detector with high performance," *Phys. Med. Biol.*, vol. 64, no. 10, May 2019, p. 10LT01, doi: 10.1088/1361-6560/ab1ba0.